POLITECNICO DI MILANO

Scuola di Ingegneria Industriale e dell'Informazione

Corso di Laurea Magistrale in Electronics Engineering

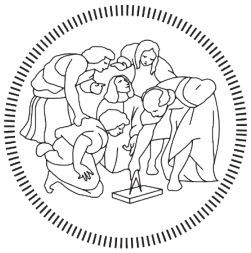

POLITECNICO
MILANO 1863

Design and Fabrication of a Multi-Parameter Biochip for Bioreactor Monitoring

Supervisor: Dr. Marco Carminati
Co-supervisors: Prof. Michael Kraft
Dr. Frederik Ceyssens

Dissertation of:

Irene Pia VINCENTINI
Matr. N. 874732

Academic Year 2017-2018

Acknowledgments

First and foremost, I would like to express my sincere gratitude to my promoters: Dr. Marco Carminati who approved this project and supported me even from afar and Prof. Michael Kraft who gave me the opportunity to develop this project in KU Leuven and gave me access to the NanoCentre cleanroom facilities. I am also extremely grateful to my co-promoter Dr. Frederik Ceyssens for sharing his extensive knowledge about microfabrication and chemistry and to his perseverance in helping me with every difficulty faced during the fabrication process. Special gratitude goes also to the Sensor Corner guys, in particular to Sina and Bram who patiently helped me every day with essential advices, to Nurul who assisted me during the measurements and to the MeBios and COK guys who kindly shared their instrumentation and knowledge.

Definitely, I would like to give thanks to Henk and all the buddies I have met in Leuven, in particular to Mattia, Pina, Marco e Dodo, Kin, for creating such a pleasant environment and memorable adventures: *dankjewel*!

I would like to warmly thank all my study (in)mates that I met during this *cumbersome* (and, please, help me say it) Master course, in particular Elena, whose strength, perseverance and encouragement helped me to succeed in my studies (*daje bro, ora si scanna*!).

Special mention goes to all the awsome people that made my days in Milan in the last six years, in particular to Dano, Fede, Manu, Salvo, Meme, Dodo, Chia, Neid, Paluc, Luke, Virgi, Cami, Vale&Cami, Charles Albert and to my special places Birrificio Lambrate, Picchio and Turnè.

I would like to express my deepest gratitude to Cler and Marti, my lighthouses in the night: at any darkest moment you were there, telling me the perfect words to get me up again. Thank you so much.

I could not have imagined having a better supporter than you, Nice. Even if we randomly met few months ago, you unexpectedly became my rock. You stood by my side, providing me with unfailing support and continuous encouragement throughout this project. You patiently listened to my whining complaints and you tenderly reassured me, as only you can. I just want to thank you for allowing me to let into your life and to find out the wonderful person you are.

Similar, profound gratitude goes to BSBE, FASK, Prodigy, Gramatik and Tasha Sultana: my studies and my research would have been impossible without their music.

Last but not the least, I would like to thank my family, in particular to my parents who supported me throughout my studies, to my brother Stefano whose wisdom has always surprised me, to my grannies Fiumana and Netta's never-ending pride (and *orecchiette*) and to uncle Alfred, aunts Dona and Anna, Riccardo and Semola who have always been able to make me feel home (don't worry, you won't get rid of me that easy: I will always send you parcels).

Bianca and Marco, you deserve a special mention, because you are more than family and friends: you are my life. You have been a sister, a brother, a friend, a partner in crime, a confidant, everything. You changed my life completely and for that I will always be grateful. Bianca, we've grown up together and you will always be my *cuggi*. Marco, even if professional choices will split us apart, *tedium* will always bind us.

Contents

Abstract

Bioprocesses monitoring has always generated great interest in biotechnology. Nowadays devices that provide real-time data are highly required, since they allow detecting small changes quickly, adjusting relevant parameters and maintaining the process at its optimum. Moreover, researchers are interested in monitoring several parameters all at once: this has led to the development of multi-sensor lab-on-a-chip (or biochip) devices.

The aim of this master's thesis was to introduce a multi-sensor chip capable of monitoring six of the most important bioprocess parameters: glucose, lactate, cell density, pH, dissolved oxygen and temperature.

In the first part of this thesis work, a general introduction on multi-sensor biochips is presented. Afterwards, a complete theoretical analysis of each of the sensors related to the aforementioned parameters was discussed in details, focusing on the various electrochemical detection techniques.

After designing, the chips were fabricated using standard microtechnology techniques in the cleanroom of the KU Leuven ESAT-MICAS department: platinum, gold and silver electrodes were produced by performing sputtering and lift-off; isolation layers of either parylene-C or polyimide were etched by reactive ion etching (RIE) after being respectively deposited by chemical vapor deposition (CVD) and spin-coated.

Subsequently, sensors were functionalized, characterized and tested using either impedance spectroscopy or electrochemical detection techniques, like amperometry and potentiometry. Finally, the response of single sensors was investigated and good performance were obtained, comparable to those described in literature.

Sommario

Il monitoraggio dei processi biologici ha sempre assunto un ruolo di fondamentale importanza in ambito biotecnologico. Oggigiorno la necessità di dispositivi in grado di fornire dati in tempo reale è diventata sempre più esigente, dal momento che permettono di rilevare velocemente piccoli cambiamenti dei parametri vitali e di monitorarli correttamente. Oltretutto, è di grande interesse tenere sotto osservazione diversi parametri simultaneamente: ciò ha spinto alla diffusione di dispositivi multisensori noti come *lab-on-a-chip* o più comunemente *biochip*.

L'obiettivo di questa tesi è quello di presentare un chip multisensore in grado di monitorare sei tra i più importanti parametri studiati nei bioprocessi: glucosio, lattosio, densità cellulare, pH, ossigeno e temperatura.

Nella prima parte del lavoro, è presentata un'introduzione generale riguardante i biochip con multisensori. Successivamente, è seguita una dettagliata analisi teorica di ognuno dei sensori associati ai parametri elencati precedentemente, focalizzandosi sulle varie tecniche di rilevazione elettrochimica.

Al design dei vari chip è seguita la produzione nella cleanroom del dipartimento ESAT-MICAS dell'università KU Leuven, utilizzando tecniche di microfabbricazione standard: elettrodi in platino, oro e argento sono stati realizzati tramite *sputtering* e *lift-off*; layer isolanti in parylene-C o poliammide sono stati depositati tramite *chemical vapor deposition* (CVD) e modellati tramite *reactive ion etching* (RIE).

Successivamente, funzionalizzazione, caratterizzazione e testing dei sensori sono stati eseguiti utilizzando tecniche di spettroscopia di impedenza, amperometria e potenziometria. Infine, è stata studiata la risposta dei singoli sensori e sono stati conseguiti risultati analoghi a quelli ottenuti in letteratura.

Chapter 1

State of the Art

In this chapter an overview of the state of the art on the different sensors is given. Many examples of applications are presented, with an introduction on multi-sensor biochips and their demand in biotechnological fields.

1.1 Introduction and Objectives

In biotechnology, in order to meet key requirements as high efficiency and product quality, precise process control is crucial. Nowadays there is also increasing interest in the use of devices that allow real-time monitoring of bioprocess parameters [1]. The development of lab-on-a-chip (or biochip) devices for biochemical analysis has seen an explosive growth over the past decades, since it provides real-time data which allows detecting small changes quickly, adjusting relevant parameters and maintaining the process at its optimum [2, 3].

The key parameters that are usually monitored and controlled in industrial-scale suspension cultures are concentration of nutrients (e.g., glucose) and metabolites (e.g., lactate), pH, temperature, dissolved oxygen and carbon dioxide and product parameters like cell density or concentration of enzymes, antibodies, vaccines, etc. [1, 3].

In literature, a considerable number of different types of sensors for all of the mentioned parameters exists. Though they are typically designed to measure single

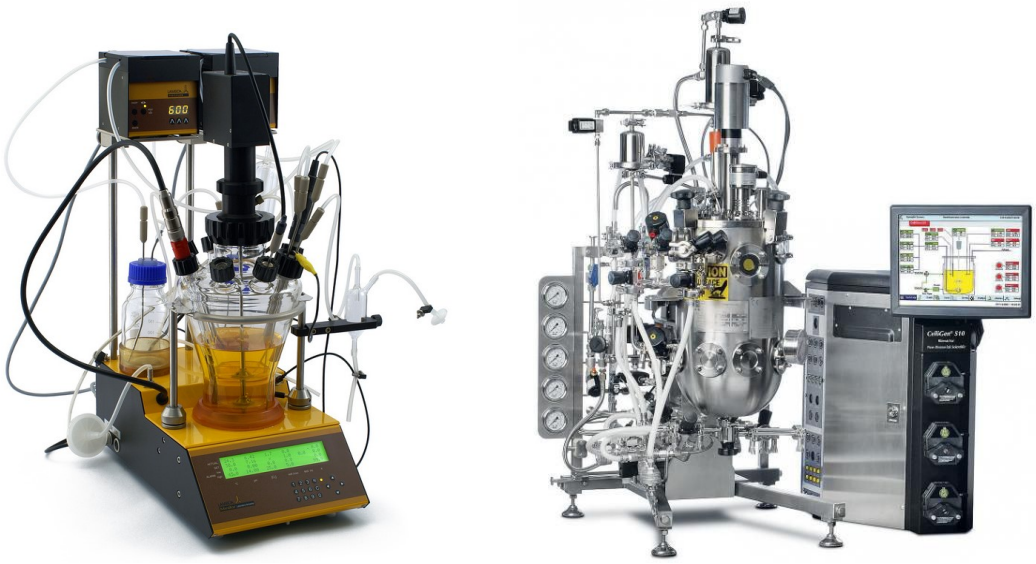

(a) (b)

Figure 1.1: Industrial fermentors with multiple single sensors. The setup is complicated, requires much space, bears the risk of contamination and increases costs.

parameters individually, in biotechnological fields researchers are barely interested in monitoring individual parameters. This would lead to the use of multiple single sensors that would occupy a considerable installation space, at the expense of the area designated to cultivation. Specifically, in the case of small bioreactors, such as cell culture flasks, sensors in large housings may not be applicable at all (Fig. 1.1). Moreover, other drawbacks introduced with the adoption of multiple single sensors are the risk of contamination and the increased costs. This last aspect is enhanced, for example, for single-use bioreactors, which are increasingly in demand in biochemical applications. Multi-sensor systems provide a viable solution to all these drawbacks: they offer a simultaneous monitoring of a wide range of parameters, since now sensors may be significantly smaller, simpler to use and more cost-effective than multiple single sensors [4, 5].

Moreover, thanks to the close proximity of the integrated sensors, all parameters are measured virtually at the same spot. This allows making the signals of the individual sensors more robust and reliable by considering the data of the other

sensors [3]. As an example, sensors signals could be compensated with temperature and pH measurement, since they significantly influence them. Furthermore, data of several sensors may be used to derive the same process parameter to confirm sensor data, for example cell density from a cell density sensor and glucose and lactate levels [6].

Several multi-sensor works exist [7, 8, 9, 10, 11], but they are focused only on a few number of different sensors. In this thesis, a multi-sensor system for the parallel in-situ monitoring of glucose, lactate, cell density, pH, oxygen and temperature in biotechnological processes is presented. These parameters are chosen since they play a meaningful role in monitoring a wide range of bioprocesses. Glucose is one of the main nutrients for a broad range of cell and microbial cultures and as such plays a key role in biotechnology. Glucose concentration monitoring is of major importance for keeping cells at the optimal point in their metabolic activity [3]. Lactate is one of the key metabolites secreted by mammalian cells and gives information about the health of the cells and their metabolic activity [12]. The cell density is of interest in processes where cells are the final product as well as in those where metabolites are harvested [13]. The pH is a crucial reactor parameter, especially in mammalian cell cultures where it has to be maintained in tight boundaries to ensure proper cell metabolism and high quality of the metabolic products [14, 15]. A process parameter of equal importance as the previously discussed ones is temperature, since it has a significant influence on cell growth and production rate [16, 17, 18, 19]. Finally, dissolved oxygen (DO) sensing has been frequently used to monitor the cellular metabolic activity and rapidly determine cell viability. Adequate supply of oxygen plays a key role in cell proliferation and differentiation and abnormal supply of oxygen may lead to a diseased state [20].

This integration of single sensors leads to some distinct advantages, as that the bioreactor setup is simplified and space and costs are reduced [3].

The aim of this master's thesis is to overcome the drawbacks presented by multiple single sensors, introducing a multi-sensor chip capable of monitoring six of the

most important process parameters in bioprocesses: glucose, lactate, cell density, pH, dissolved oxygen and temperature.

1.2 Glucose and Lactate Sensors

Biosensor chips, especially those based on electrochemical detection, have been abundantly developed in the past decades [21]. The most popular electrochemical biosensors are the enzyme-based electrodes, since they offer several advantages like high specificity towards their target molecules, long-time stability when kept in an appropriate environment, various immobilization methods and commercially availability for a wide variety of substrates [22]. Enzymes are proteins that catalyze a reaction with high specificity for their target molecule, making reactions occur faster and with lower activation energy. The catalysis of the chemical reaction takes place at the active site of the enzyme and its conformation is accountable for the high specificity of the enzyme [22].

In bioprocesses monitoring, the main analytes to be measured are glucose and lactate. The first one has a key role in the production of glycoproteins in mammalian cell cultures, in the maintenance of optimum conditions for cell growth in yeast cell cultures and in preventing stuck fermentation and substrate inhibition (i.e. if the glucose concentration exceeds a certain threshold, yeast cells start to metabolize the nutrient anaerobically) [9]. Similarly, lactate is one of the main metabolites in mammalian cell cultures and gives information about the health of the cells and their metabolic activity [23].

The enzymes used in this work were the glucose oxidase (GOx) and the lactate oxidase (LOx), because of their low cost, high specific activity and reliability [24]. The reaction equation for the enzymatic conversion of glucose by glucose oxidase is as follows [25]:

$$\beta\text{-D-glucose} + \text{GOx} + \text{O}_2 \longrightarrow \delta\text{-D-gluconolactone} + \text{H}_2\text{O}_2. \tag{1.1}$$

Similarly, for lactate oxidase the reaction can be written as [26]:

$$\text{L-lactate} + \text{LOx} + \text{O}_2 \longrightarrow \text{pyruvate} + \text{H}_2\text{O}_2. \tag{1.2}$$

The enzyme kinetics is influenced by several parameters, such as temperature, pH, immobilization technique and diffusion-limiting membranes [27]. A key role in the glucose and lactate detection is played by the oxidizing agent or "redox mediator", which in this case may be assumed to be the hydrogen peroxide H_2O_2. After the reaction of the enzyme molecule with its substrate, the redox mediator can convert the enzyme back into its native form, making it ready for conversion of the next substrate molecule. In order to translate the enzymatic reaction into an electrical signal, amperometry is used because of its straightforward detection scheme and the widespread availability of affordable laboratory instruments [9].

1.2.1 Amperometric Enzyme Sensors

Since the last decades, electrochemistry has been playing an important role in a vast number of fundamental research and applied areas. Bard and Faulkner defined it as “the branch of chemistry concerned with the interrelation of electrical and chemical effects” [28]. Actually, chemical reactions that occur between an electronic conductor (an electrode) and an ionic conductor (an electrolyte) lead to a charge movement and so to an electric current passage. These reactions are known as reduction-oxidation or redox reactions.

Electrochemical reactions are monitored and quantified in a three or two electrode setup controlled by a potentiostat, an electronic instrument capable of measuring and controlling voltage and current flows between different electrodes. A three-electrode system (Fig. 1.2) consists of a working electrode (WE), a counter electrode (CE) and a reference electrode (RE) [9]. The WE, that is the functionalized electrode, is held at a stable and known potential relative to the RE one, which is independent of any chemical activity in solution. The potentiostat either provides or drains current needed to keep the WE at the desired potential through the CE.

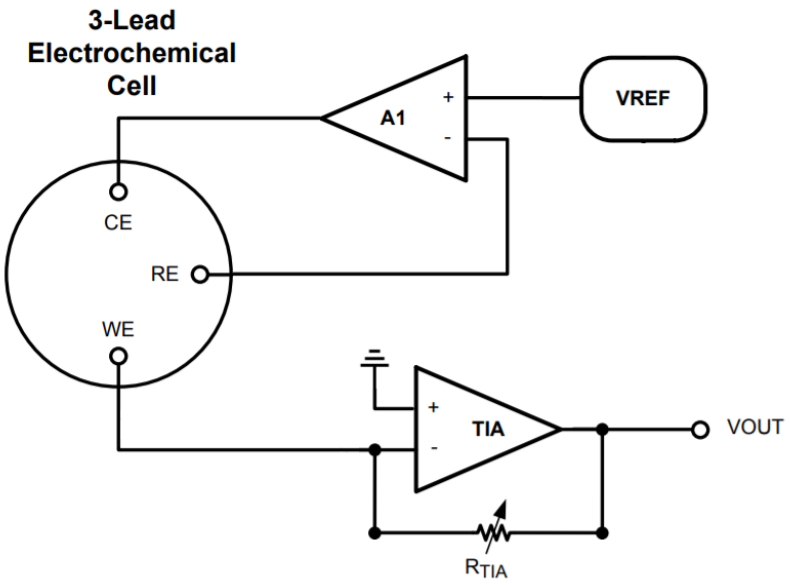

Figure 1.2: Schematic representation of a potentiostat circuit.

The WE and the CE are typically made of biocompatible, inert and highly conductive materials like gold or platinum, whereas the RE is an Ag/AgCl electrode. The device used to measure the potential difference between the WE and the RE has ideally a high input impedance, so that no current is drawn through the RE. In real measurement, though, a small current is always present, hence in order to have as small electrolyte conductivity influences as possible, the RE should be positioned in close proximity to the WE [28, 29]. Moreover, in order to neglect the CE double-layer capacitance and to ensure the least possible potential drop between CE and WE, it's better to design the CE area bigger than the WE one.

Concerning glucose and lactate redox reactions, if a sufficient relative potential at the WE is applied, the redox reaction rate reaches a maximum value and the reaction taking place at the WE can be written as:

$$H_2O_2 \longrightarrow 2e^- + O_2 + 2H^+ \tag{1.3}$$

Under this condition, the current detected by CE and WE depends only on the rate of mass transfer of the redox species from the bulk solution to the electrode.

This condition is described by the Cottrell equation [28, 29]:

$$I = \frac{nFAC\sqrt{D}}{\sqrt{\pi t}} \tag{1.4}$$

where n is the number of electrons implied in the redox reaction, F the Faraday constant (96485 sA/mol), A the surface area of the electrode, C the concentration of the redox species, D the diffusion coefficient in the solution, t the time. The Cottrell equation is derived from Fick's second law of diffusion and predicts the variation of the current in time, when a potential step is applied under conditions of large overpotential [29]. Under these conditions, the current should become zero after a relatively long time: this may be explained considering the spread of redox specie around the electrode and this leads to longer diffusion distances. Nonetheless, a steady state value of the current may be reached if a membrane on top of the electrode is considered [22]. In this case, mass transport to the electrode surface is controlled by diffusion through this layer and a constant flux to the electrode can be assumed since the depleted layer cannot spread further than the distance to the inner membrane surface (i.e., the concentration of the redox species on the inner side $C_i = 0$).

Under these considerations, the Cottrell equation becomes:

$$I = nFA\frac{D}{l}C \tag{1.5}$$

where l is the membrane thickness. Using this equation, the current flowing through the membrane onto the functionalized electrode can be predicted.

1.2.2 Kinetics of Enzymatic Reaction

The general form of an enzymatic reaction is written as [30]:

$$\mathrm{E} + \mathrm{S} \rightleftharpoons \mathrm{ES} \longrightarrow \mathrm{E} + \mathrm{P} \tag{1.6}$$

where E denotes the enzyme, S its substrate, ES the enzyme-substrate complex

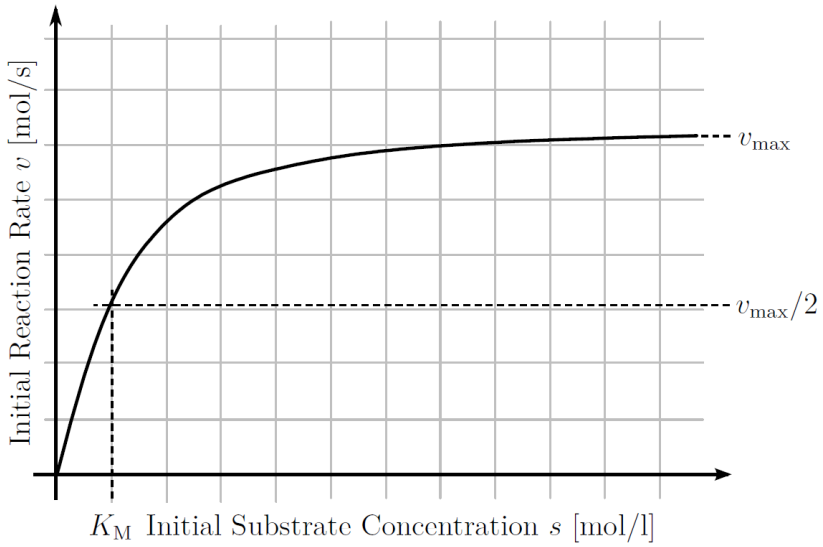

Figure 1.3: Michaelis-Menten kinetics: relationship between substrate concentration s and product formation rate v; up to K_M, the relationship can be considered linear.

and P the product. The kinetics of enzymatic reactions can be described by the Michaelis-Menten equation that relates the rate of product formation v [mol/s] to the substrate concentration s [mol/l]:

$$v = \frac{v_{max} s}{K_M + s}, \tag{1.7}$$

where v_{max} is the maximum reaction rate that depends on the enzyme concentration and activity and K_M is the Michaelis-Menten constant. This last parameter is a very helpful quantity that measure the affinity of the enzyme to its substrate.

The initial rate of reaction v can be plotted as a function of the initial substrate concentration s in order to determine K_M and v_{max}. As shown in Fig. 1.3, the curve is a hyperbola that tends to the asymptotic value v_{max} for $s \to \infty$ and has a quasi-linear behavior up to $s = K_M$, where half of the maximum product formation rate is reached. If this linear approximation is considered, the relationship between v and s can be described by a first-order equation:

$$v = \frac{v_{max} s}{K_M}. \tag{1.8}$$

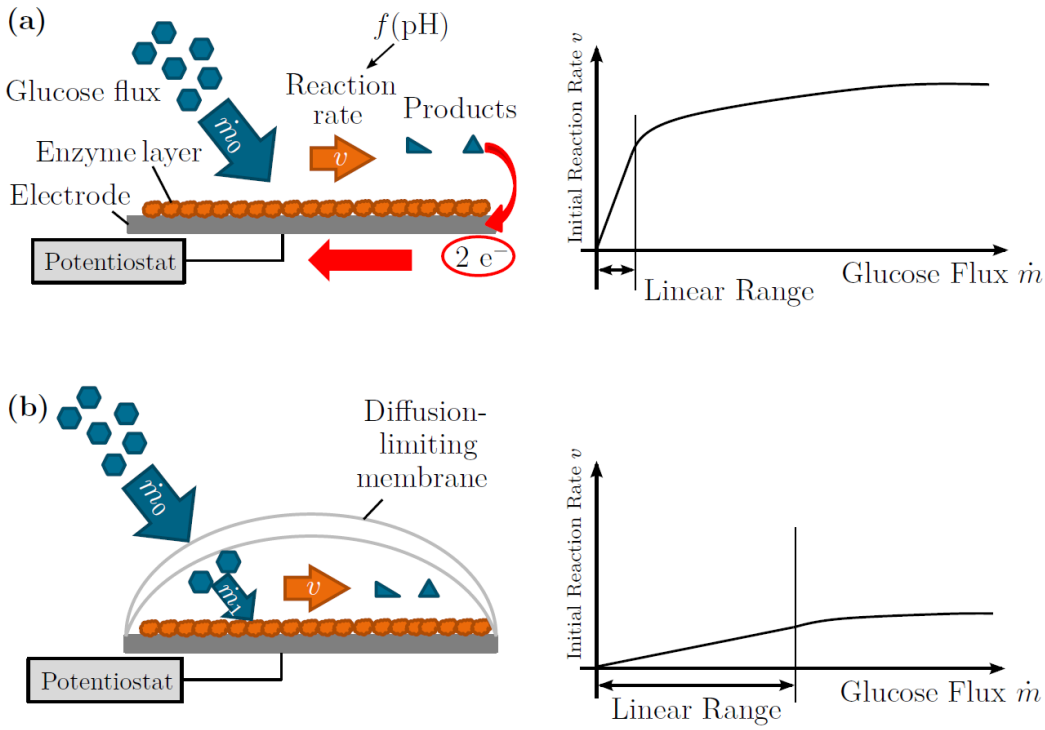

Figure 1.4: Extension of the linear measurement range of a glucose sensor: (a) unhindered flux of glucose molecules to the enzyme layer results in fast saturation of the reaction rate; (b) diffusion-limiting membrane reduces arriving glucose molecules per time and extends linear range.

The Michaelis-Menten constants for glucose oxidase and lactate oxidase are around 33 mM and 0.7 mM respectively [23]. Concentration ranges of glucose and lactate in bioprocesses go up to around 50 mM for mammalian cell cultures, but can reach values up to 1000 mM in the production of biodegradable polymers and 1500 mM in alcoholic fermentation [23]. This means that an enzyme sensor by far does not cover the relevant concentration ranges found in bioprocesses.

A practical way to achieve wide linear ranges for enzyme sensors is the application of a membrane onto the functionalized electrode surface, reducing the flux of analyte molecules to the enzyme, thereby assuring an analyte concentration $s << K_M$ at the enzyme layer (Fig. 1.4) [31, 23, 32]. Furthermore, the integration of a membrane adds several benefits, such as protection of the enzyme layer against hostile environmental influences and interfering substances, assuring stable signals over a period of several

days or weeks.

A thorough mathematical description of the transport phenomena in enzyme sensors with diffusion-limiting membranes is derived in Mross' dissertation, where the transport and reaction processes occurring in the membrane and the enzyme layer are taken into account [22]. Combining Fick's laws with the Michaelis-Menten equation, the upper limit of the linear measurement range of the enzyme sensor S can be estimated as:

$$S = \frac{v_{max} l_e l_m}{2 K_M D_m} + 1, \tag{1.9}$$

where l_e and l_m are respectively the enzyme layer and membrane thicknesses and D_m is the diffusion coefficient of the substrate in the membrane.

Among various materials that have been used for diffusion-limiting membranes like cellulose acetate [33], PDMS [9], polycarbonate [34] and Nafion® [35, 36], polyurethane (PU) was chosen in this work due to its biocompatibility and permeability for oxygen, glucose and lactate [31, 23].

In order to develop the PU membrane, PU pellets have to be dissolved in mixtures of the solvents tetrahydrofuran (THF) and dimethylformamide (DMF). Noticeably, the PU concentration and the THF:DMF ratio affect some membrane properties like morphology and permeability, that is, more specifically, porosity and tortuosity [23].

1.3 Cell Density Sensor

Measurement of the cell density is essential for accurate bioprocesses monitoring. Conventional techniques used for detecting this parameter include weighing of dried cells, manual or automated cell counting and optical methods [3]. Though, these techniques are either inaccurate or require cumbersome and expensive instruments, hence in-situ measurements and sensors miniaturization and integration are impossible to achieve [7, 8]. Moreover, an indispensable accomplishment demanded by a cell density sensor is the ability to distinguish between live and dead cells. In

fact, as an example, even though optical methods are very powerful and precise in detecting cells, their ability in making this distinction lays on cell morphological analysis which may be quite unreliable.

A method that overcomes these aforementioned limitations is impedance spectroscopy. Its working principle relies on live cells membrane polarization occurring in an electric field. Indeed, dead cells don't possess intact plasma membranes and, consequently, their polarization is completely negligible [7, 8]. Hence, an alternating current (AC) electrical field is applied to the cell culture and when the frequency exceeds the so called characteristic frequency f_{char}, the interfacial polarization of the cell membrane is not more able to follow the electric field [37]. This characteristic frequency above which polarization does not occur anymore depends strongly on cells shape, membrane capacitance and conductivity and background electrolyte conductivity [7]. Therefore, the overall solution impedance can be evaluated, as the conductivity is measured as a function of the frequency.

Several models for different cell geometries have been developed [37, 38]. Yeast cells are commonly modeled as single shell spherical cells [37]. Precisely, the relationship between the conductivity change $\Delta\sigma$ and the viable cell density N_c for spherical cells has been derived as [37]:

$$\Delta\sigma \approx 6\pi r^3 N_c \sigma_a \left(\frac{\sigma_i/\sigma_a}{2 + \sigma_i/\sigma_a} \right) \tag{1.10}$$

with r being the cell radius and σ_i and σ_a the conductivity of the cell cytoplasm and background electrolyte conductivity respectively.

1.3.1 Impedance Spectra Analysis

Before dealing with the electrode design, it's better to inspect which factors influence the frequency response, so to outline a proper model for the impedance spectra analysis. As depicted in Fig. 1.5, an equivalent circuit diagram and its corresponding impedance spectrum can be derived, considering the following main factors [39]:

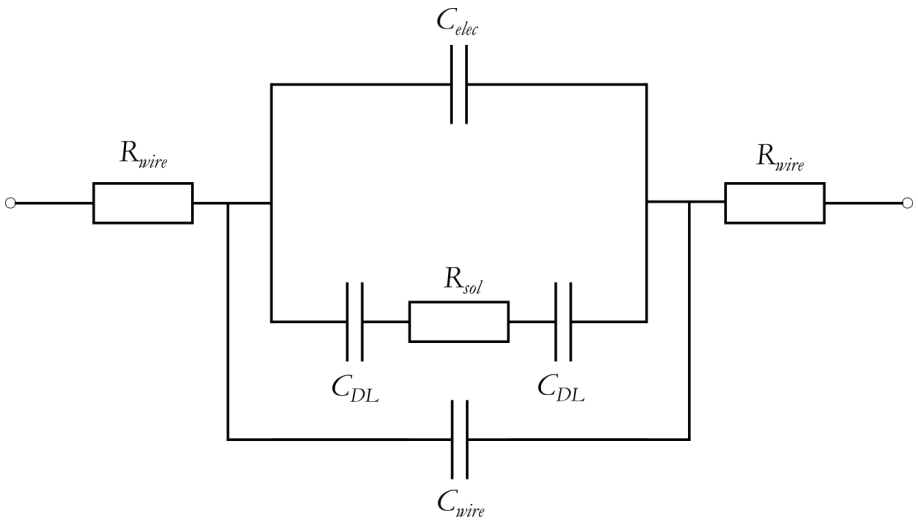

Figure 1.5: Equivalent circuit diagram of electrodes in an aqueous solution; C_{DL}: capacitance of electrical double layer, C_{elec}: capacitance between electrodes, R_{sol}: solution resistance, R_{wire}: wiring resistance, C_{wire}: wiring capacitance.

- the capacitance of the electrical double layer on the electrodes C_{DL}
- the capacitance between the electrodes C_{elec}
- the solution resistance R_{sol}
- the wiring resistance R_{wire}
- the wiring capacitance C_{wire}.

The impedance of the equivalent circuit $Z = |Z|$ can be calculated as:

$$\begin{aligned} Z &= 2R_{wire} + (Z_{cell}||(2Z_{DL} + R_{sol})) \\ &= 2R_{wire} + \left(\frac{1}{\omega C_{elec}}|| \left(\frac{2}{\omega C_{DL}} + R_{sol}\right)\right) \\ &= 2R_{wire} + \frac{2/\omega C_{DL} + R_{sol}}{(2/\omega C_{DL} + R_{sol})\omega C_{elec} + 1}. \end{aligned} \tag{1.11}$$

The corresponding impedance spectrum shows an ohmic plateau at middle frequencies, delimitated by two cutoff frequencies f_{low} and f_{high}, as shown in Fig. 1.6. The equivalent impedance at low frequencies (i.e. $f < f_{low}$) is dominated by the capacitance of the electrical double layer C_{DL} formed on each electrode, that explains

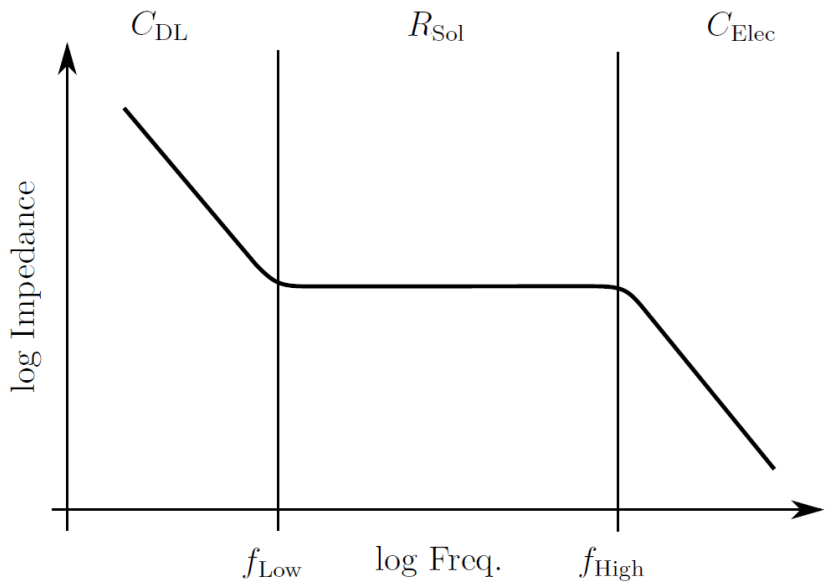

Figure 1.6: Schematic impedance spectrum of electrodes in an aqueous solution with the two cutoff frequencies f_{low} and f_{high} and the ohmic plateau in between.

the interface phenomena at the electrode-electrolyte interfaces [40]. Since the double layer capacitive effect is present on each electrode, a double contribution should be considered in the lower cutoff frequency estimation:

$$f_{low} \approx \frac{1}{\pi R_{sol} C_{DL}}. \tag{1.12}$$

The ohmic behavior in the middle region of the impedance spectrum (i.e. $f_{low} < f < f_{high}$) is basically due to the solution resistance R_{sol} alone, since the double layer capacitance contribution becomes negligible and the capacitance between the electrodes poses a too big impedance yet.

Finally, at high frequencies (i.e. $f > f_{high}$) the contribution of the capacitance between the electrodes C_{elec} prevails. In this part, the parasitic wiring capacitance C_{wire}, estimated as approximately 100 pF/m [22], has to be considered in parallel to C_{elec}. Therefore, the lower cutoff frequency is derived:

$$f_{high} \approx \frac{1}{2\pi R_{sol}(C_{elec} + C_{wire})}. \tag{1.13}$$

1.4 pH Sensor

pH is one of the key parameters in biotechnological processes, since it has a significant impact on cells microenvironment and homeostasis [14]. Process performance and product quality may be controlled monitoring cellular respiration waste products, as carbon dioxide and organic acids, which influence environmental acidity [1]. For that reason, active pH control helps studying cell growth rate, viability and synthesis of metabolic products [41].

Over the years, several methods to measure pH have been analyzed. The paper-based colorimetric method, where pH is visually identified through the color of the paper, and the glass electrode were the first ones [42]. In the last decades, new methods have been investigated in order to overcome drawbacks introduced by those last ones, as high inaccuracy in the first case and fragility and high cost in the second one. Therefore, electrochemical pH sensors have taken over. They are suitable to be integrated in miniaturized setups and reliable results have been demonstrated [42, 43].

Electrochemical pH sensors can be categorized into three types according to their sensing mechanism, that could be either chemical, physical or hybrid as combination of both. While in chemical methods protonation/deprotonation, doping/de-doping and redox reactions occur between the sensing materials and hydronium ions, the physical sensing mechanism is based on charge depletion/accumulation [42]. Although chemical techniques have a limited maximum sensitivity governed by the Nernst equation, their working principles set up on completely reversible reactions. On the other hand, pH sensors based on ion-sensitive field-effect transistor (ISFET) technology show very high sensitivity ranges, even if they suffer from an initial drift, are not suitable for long-term measurements and present weak chemical stability (i.e., oxide dissolution of the electrodes in highly alkaline or highly acidic media) [42, 43, 44].

In this work, a potentiometric sensing method based on electrochemical mechanisms was used, since it's stable, continuous, low-cost and easy-to-use [43].

1.4.1 Potentiometric pH Sensing

pH is defined as the decimal logarithm of the reciprocal of the hydrogen ions activity, a_{H^+}, in a solution [45]:

$$pH \triangleq -\log_{10}(a_{H^+}). \tag{1.14}$$

In order to detect hydrogen ions activity, polymer-based sensors are generally used in clinical and biological applications [46]. Commonly used hydrogen selective polymers are polypyrolle, polyaniline and poly(1-aminoanthracene) [42]. Electropolymerization steps allow polymers to be tightly bound to the electrode surface and ready to be protonated/deprotonated by hydrogen ions.

The standardized way to extract signals from those kinds of sensors is by potentiometric sensing [42, 43, 44]. A typical potentiometric sensor has a two-electrode structure: the working electrode (WE) having the sensing polymerized surface and an Ag/AgCl reference electrode (RE). When both electrodes are plunged in an electrolyte solution, the transport of charge across the interface between chemical phases lead to an electrical potential drop across the electrodes. This potential difference is taken as a measure for determining H^+ ions concentration in the solution and consequently the pH [43].

The polymer film on top of the WE acts as an ion-selective membrane and the H^+ ions flux across the membrane generates the potential difference, that can be quantitatively determined by the Nernst equation [28]:

$$E = constant + \frac{RT}{z_i F} \ln(a_i^{sol}) \tag{1.15}$$

where R is the gas constant (8,314 J/K mol), T the absolute temperature, z_i the charge of the primary ion (H^+ in this case), F the Faraday constant and a_i^{sol} the activity of the primary ion in the sample (by definition, the "activity for species i" refers to the concentration of i multiplied by the mean ionic activity coefficient). The constant term is the sum of potential differences at all of the other interfaces featuring phases of constant composition, so including H^+-activity-independent terms.

It is evaluated by measuring the potential across the cell in which the test solution is replaced by a standard solution having a known activity for species *i*. Hence, considering a constant temperature value of 25° C and $z_{H^+} = 1$, recalling the definition of pH (Eq. 1.14) and converting the natural logarithm to the decimal one, we can rewrite the previous equation as:

$$E = constant - 59.1mV \cdot pH \tag{1.16}$$

where 59.1 mV is defined as the sensitivity S.

1.5 Dissolved Oxygen Sensor

Dissolved oxygen (DO) refers to the amount of gaseous oxygen dissolved in the water, which is readily available to living organisms by direct absorption from the atmosphere or as a waste product [47]. In biological processes, dissolved oxygen concentration is an important parameter to be monitored. For example, cells metabolism and activity are marked by the respiration rate. Since live cells have always an absolute demand for oxygen, this parameter detection can lead to cell differentiation and cell growth processes [1]. Typically, the DO sensor and the cell density sensor results may be compared to obtain more reliable and robust measurements.

1.5.1 UMEA

Nowadays, different electrochemical and optical techniques are used for the measurement of DO: the most common are amperometry, optical technology and laser spectroscopy [48]. The last two are relatively new technologies based on fluorescence and light absorption and, though they have seen widespread adoption due to its inherent stability, their applications are limited by the complicated fabrication and expensive sensing apparatus [20].

Alternatively, electrochemical measurements have been successfully and widely used for decades in a variety of applications. The first experiments were conducted by Clark in 1953, where he described an amperometric procedure to determine in vitro oxygen in blood [49, 50]. The Clark-type electrode consists of a platinum cathode where oxygen reduces and a silver anode where oxygen oxidases. Those electrodes are conductively connected via an electrolyte solution and separated by an oxygen permeable membrane from the measurement solution [48, 20]. The Clark-type oxygen sensor has been applied in clinical analysis, fermentation monitoring and biosensor development, due to easy fabrication, low cost, good repeatability and reproducibility and fast response. However, those sensors are unsuitable for use in clinical work since they suffer from design specific problems, e.g., relatively big size and poor spatial resolution, and the consumption of dissolved oxygen at the cathode may change the local oxygen concentration [20].

Against this backdrop, microelectrodes and ultramicroelectrodes array (UMEA) were proposed as reliable and accurate oxygen sensors alternatives and used as working electrodes in amperometric techniques [7, 8, 51]. By definition [29], an ultramicroelectrode (UME) has a diameter less than 25 μm, hence, not only the electrode size is certainly scaled down, but the amount of oxygen consumed by the electrochemical sensor is definitely reduced as well. The main disadvantage of UMEs is the low detected current, that may be covered by a background noise, but if an array of UMEs is used, the total current signal is given by the sum of each UMEs current. Thus, in UMEAs the active electrode area is reduced while maintaining a total sensor surface comparable in size with the counter and reference electrodes used in the amperometric measurement.

Both theoretical and experimental works [52, 53, 54, 55, 56] respectively described and confirmed mass transport models in several geometrical (e.g., spherical, disk, ring, band) and structural (inlaid or recessed) configurations. A complete model of the disk UME current response is given by Bard and Faulkner [28], who solved the diffusion equation based on Fick's second law for the inlaid disk geometry,

obtaining the following current-time curve:

$$i(\tau) = \frac{4nFAD_O C_O}{\pi r_O} f(\tau) \tag{1.17}$$

where n is the number of electrons involved in the reaction, F the Faraday constant, A the surface area of the electrode, D_O and C_O respectively the diffusion constant and the initial concentration of the electro-active species, r_O the disk radius. The function $f(\tau)$ was determined as two series applicable in different domains of the variable τ, with $\tau = 4D_O t/r_O^2$.

At short times, i.e. $\tau < 1$, considering the first order approximation, the Cottrell equation is derived:

$$i(t)_{short\,times} = \frac{4nFAD_O C_O}{\pi r_O} \frac{\sqrt{\pi}}{2} \sqrt{\frac{r_O^2}{4D_O t}} = \frac{nFA\sqrt{D_O} C_O}{\sqrt{\pi t}}. \tag{1.18}$$

At long times, i.e. $\tau > 1$, at the first order approximation, the steady state current is expressed as:

$$i(t)_{ss} = \frac{4nFAD_O C_O}{\pi r_O} = 4nFD_O C_O r_O. \tag{1.19}$$

From a structural configuration point of view, Bond et al. presented in detail a comparison of the chronoamperometric response at inlaid and recessed disk microelectrodes [52]. As shown in Fig. 1.7, in both configurations a circular metal disk is surrounded by an insulating medium, but while in the "inlaid" arrangement it forms a geometric continuation of the electrode plane, in the "recessed" one it does not. The basic differences between the two configurations are the following:

- The steady state current of the recessed disk is smaller of a factor $4h/\pi r_O$ than that of the inlaid one.

- The inlaid disk has a very slow transition of the from Cottrellian to steady-state behavior, whereas the recessed disk almost "switches" from one regime to the other.

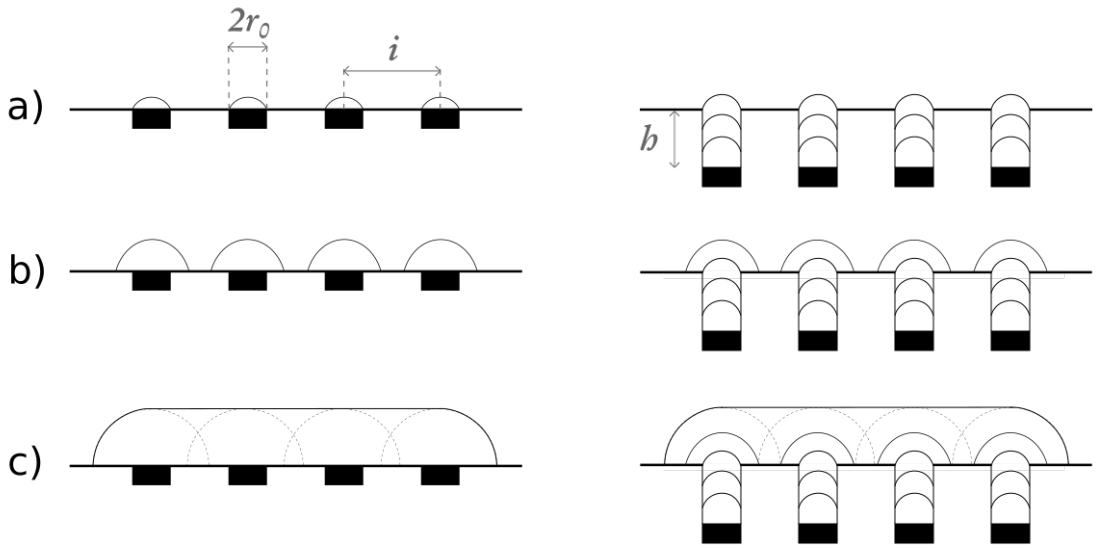

Figure 1.7: Schematic representation of diffusion layers of concentration profiles developing at arrays of electrodes (inlaid at the left, recessed at the right) with a radius r_0, an interelectrode distance i and a recession height h. Three different times of the electrochemical perturbation are considered: (a) planar diffusion at short times, (b) hemispherical diffusion at intermediate times and (c) planar diffusion and overlap of individual diffusion layers at longer times.

- The ohmic polarization during chronoamperometric experiments is much more severe for a recessed disk than for an inlaid one of identical area.

Bond et al. [52] derived the recessed disk UME model from the inlaid one, where both unstirred and stirred solution cases are evaluated. In the first situation, the steady state current is written as:

$$i_{recessed,unst,ss} = \frac{4\pi r_O^2 nFD_O C_{O,b}}{4h + \pi r_O} \tag{1.20}$$

where h is the recess depth. When stirring occurs, convection maintains the electrode tube edge concentration equal to the bulk solution one. Under this assumption, the steady state current is evaluated as:

$$i_{recessed,st,ss} = \pi nFD_O C_{O,b} \frac{r_O^2}{h}. \tag{1.21}$$

Whereas, considering the first order approximation, the short-times behavior is always given by Cottrell equation, irrespectively of whether there is convection or not.

Considering now the UMEA model, the overall response is not only related to the concentration of the electroactive species in solution, but it also depends on some geometrical parameters, such as the inter-electrode distance, the number of UMEs and the density of the electrode distribution. A schematic representation of the diffusion layers of concentration profiles is shown in Fig. 1.7, as illustrated by Zoski [29]. When the duration of the experiment is sufficiently short for the diffusion layer to be small with respect to the radius of the electrodes (Fig. 1.7.a), each UME exhibits a Cottrellian behavior, hence the UMEA can be treated as a series of m independent UMEs:

$$i(t) = \frac{mnFA_{el}\sqrt{D_O}C_O}{\sqrt{\pi t}}. \tag{1.22}$$

where m is the number of UMEs and A_{el} the area of the individual active elements.

At longer times, the individual diffusion layers become larger than the electrode dimensions. If the inter-electrode distance is still larger than the size of the diffusion layers, a quasi-steady-state diffusion takes place at each element (Fig. 1.7.b). The current still depends on the sum of the currents at each UMEs, but is proportional to a factor $\delta(d)$, which depends on the shape of the electrodes and to the equivalent diffusion layer thickness d:

$$i(t) = \frac{mnFA_{el}D_OC_O}{\delta(d)}. \tag{1.23}$$

In the specific case of a UMEA with recessed electrodes, the $\delta(d)$ model has been studied in previous work [29, 51]. Hence the previous equation may be rewritten as:

$$i(t) = \frac{4\pi r_O^2 mnFD_OC_O}{4h + \pi r_O}. \tag{1.24}$$

which basically corresponds to Eq. 1.20 multiplied by a factor m.

At much longer times, the individual diffusion layers overlap, resulting in an apparent global diffusion layer that extends over the array (Fig. 1.7.c). In this case,

the array behaves like a macroelectrode having an area equal to the geometric area of the entire array A_{array}, following a Cottrellian regime:

$$i(t) = \frac{nFA_{array}\sqrt{D_O}C_O}{\sqrt{\pi t}}. \tag{1.25}$$

Most of the time, the UMEA sensor is designed in such a way that the diffusion fields of the individual UMEs never overlap, otherwise all the UMEA sensors advantages would be lost.

In this work a recessed-disk-ultramicroelectrode array is reported as oxygen sensor, since mass transport (hence oxygen consumption) is reduced by an amount dependent on the height of the recess [7]. Dissolved oxygen measurements were conducted utilizing a novel ultra-short measurement protocol (ms time range) presented by van Rossem et al. [51]. They demonstrated that this combination of recessed UMEA sensor and short measurement protocol allows drastically reducing the oxygen consumption caused by the electrochemical measurements. Precisely, the time length of diffusion to reach steady state in case of recessed UMEA is calculated combining Eq. 1.24 with the Cottrell equation (Eq. 1.22):

$$t_{ss} = \frac{(4h + \pi r_O)^2}{\pi D_O} \tag{1.26}$$

Therefore, measurements should be performed with times less than t_{ss}, in order to obtain planar diffusion layers of concentration profiles, so that the UMEA response is described by the Cottrell equation for a series of m independent UMEs (Eq. (1.22)).

In order to translate the electrochemical reaction into an electrical signal, even in this case, amperometry is used due to its reliability and the need of readily available laboratory instruments.

1.6 Temperature Sensor

1.6.1 Resistance Temperature Devices (RTDs)

The resistance of metallic thin film is often used as a measure for the temperature: with raising temperature, the movement of charge carriers in the metal is subsequently induced. This happens since the resistivity of a conductive material depends on the concentration of free charge carriers and their mobility. This last parameter accounts for the ability of charge carriers to move more or less freely throughout the atom lattice [57]. As the temperature rises, the lattice vibrations become stronger, increasing the possibility of collisions among the electrons. As a consequence, the resistivity of a metal increases as well.

The physical law that relates the resistivity to the temperature takes into account the so-called positive temperature coefficient (PTC) α and is expressed as:

$$\rho_{T1} = \rho_{T0}(1 + \alpha(T_1 - T_0)) \tag{1.27}$$

where ρ_{T1} and ρ_{T0} are the metal resistivities respectively at the T_1 and T_0 temperature values. All metal resistance temperature devices (RTDs) are considered PTC sensors.

Then, considering the first Ohm's law:

$$\rho = R\frac{A}{L} \tag{1.28}$$

with R the resistance of the metal, A the cross-section area and L the total length, and combining it with the previous equation, we obtain the linear relationship between resistance and temperature:

$$R_{T1} = R_{T0}(1 + \alpha(T_1 - T_0)). \tag{1.29}$$

For more precise calculations, this equation can be expanded up to the third order. Moreover, if the nominal temperature $T_0 = 0°$ C is considered, the Callendar–Van Dusen equation is derived:

$$R_T = R_0[1 + A'T + B'T^2 + C'(T - 100)T^3]. \tag{1.30}$$

where A', B', and C' ($^*C' = 0$ for $T > 0°$ C) are the Callendar–Van Dusen coefficients. Their values for RTDs in platinum are listed in Tab. 1.1 [58], considering the most used standards:

Standard	Temperature coefficient (α)	A'	B'	C'*
DIN 43760	0.003850	$3.9080 \cdot 10^{-3}$	$-5.8019 \cdot 10^{-7}$	$-4.2735 \cdot 10^{-12}$
American	0.003911	$3.9692 \cdot 10^{-3}$	$-5.8495 \cdot 10^{-7}$	$-4.2325 \cdot 10^{-12}$
ITS-90	0.003926	$3.9848 \cdot 10^{-3}$	$-5.870 \cdot 10^{-7}$	$-4.0000 \cdot 10^{-12}$

Table 1.1: Callendar–Van Dusen coefficients corresponding to standard RTDs.

RTDs can reach accuracy values as high as 0.01 Ω at 0° C and preserve long-term stability, drifting less than 0.1° C/year [59]. This makes RTDs suitable for monitoring temperature of cell cultures in biotechnological fields, where an accuracy of ±0.5° C is typically considered adequate [18]. In principle any metal might be a potential candidate as temperature device. Though, the metal selected should have a high melting point, high resistance to corrosion, highly reproducible electrical properties and a very predictable, near-linear R–T relationship. Among the materials most commonly used for RTDs (e.g., copper, nickel, and molybdenum), platinum is by far the most adopted because of its long-term chemical stability, broad temperature range, ease of manufacture, reasonable cost and high PTC of $3.9 \cdot 10^-3° \text{ C}^{-1}$ [58]. A platinum RTD with a nominal resistance of 100 Ω at 0° C is known as Pt 100.

Since RTDs resistive values are relatively low (e.g., 100 Ω) and parasitic wire resistances have always to be taken into account, RTDs small variations can be difficult to measure. In order to overcome this problem, special configurations are introduced. As shown in Fig. 1.8, RTDs may be designed in a two-, three-, or four-wire configuration [58]. In the first and second case, a Wheatstone bridge circuit is used, since it's well suited for detecting small changes of a resistance, providing

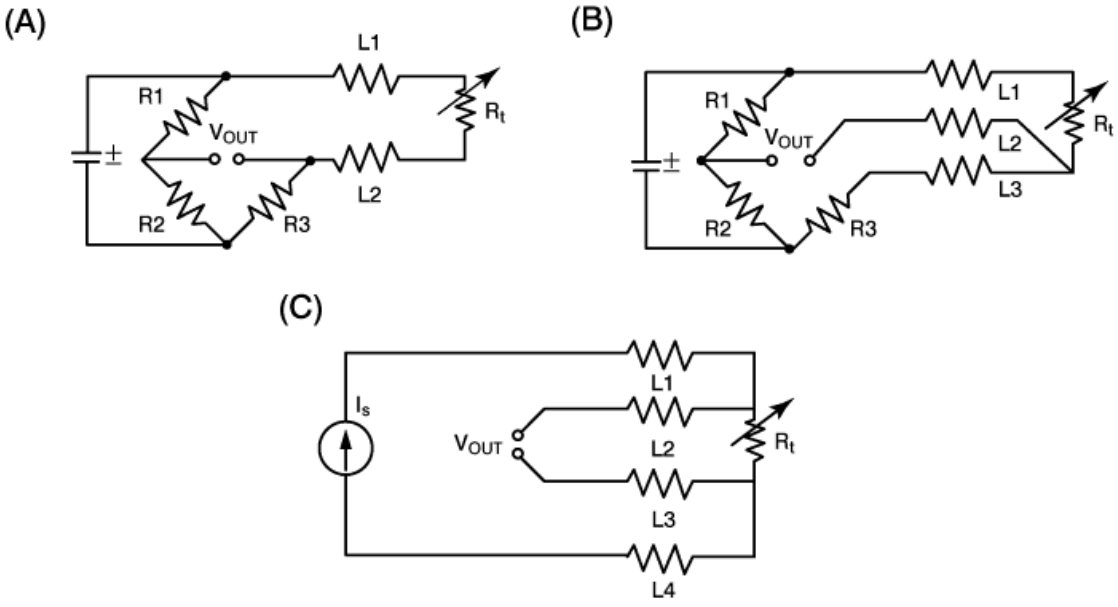

Figure 1.8: Two-, three- and four-wire configurations.

accurate measurements. While two-wire RTDs are mostly used either with short lead wires or where high accuracy is not required, three-wire RTDs are most commonly used in industrial applications, where high accuracy is achieved by measuring the resistance between lead 1 and lead 2 (L_{1+2}) and subtracting the resistance between lead 2 and lead 3 (L_{2+3}). In case of very long distances, errors caused by resistance imbalance between wires can be cancelled out in a four-wire RTD circuit [58].

Whenever an RTD is used to detect temperature variations, a current has to be injected into the device to produce a measurable voltage, since it is a passive resistive device. Its value has to be chosen properly, otherwise high currents may cause the RTD to internally heat, showing errors. This phenomenon is known as self-heating and is typically specified as the amount of power that will raise the RTD temperature by 1° C, or 1 mΩ/° C [59].

Chapter 2

Sensors Design

In this chapter the design of all sensors is introduced. Furthermore, an overview of the expected results and of the measurement setup of each sensor is given.

2.1 Glucose and Lactate Sensors

Since amperometric measurements by means of a potentiostat were carried out, a three-electrode configuration with working, counter and reference electrode was chosen. The three electrodes were arranged as concentric circles, ensuring an even distribution of the current density between the WE and the CE and an independence of the direction of flow in stirred solutions. Moreover, this circular shape made it easier to dispense the enzyme solution drops onto the WE surface. For the reasons outlined in Section 1.2.1, the working electrode was placed in the middle, surrounded by the reference and counter electrode, as depicted in Fig. 2.1.

The size of the electrodes was chosen relying upon Mross et al. work [23], where they studied the enzyme solution distribution onto the WE surface. Thus, they chose a WE diameter of 400 μm, while CE and RE had a width of 100 μm, with a spacing between the electrodes of 50 μm. Since higher electrode areas were expected to give higher currents and thus a higher sensitivity, a second variant with twice the area was designed, having a WE diameter of 566 μm, a RE/CE width of 141 μm and a spacing of 71 μm.

Figure 2.1: Design of the three-electrode setup for amperometry.

Platinum was chosen for WE and CE since it is inert, conductive and biocompatible. The RE was made of silver with a silver-chloride layer galvanically plated.

Concerning the WE functionalization, a physisorption method based on enzyme crosslinking with bovine serum albumin (BSA) and glutaraldehyde was used, since it's a very straightforward procedure and provides a comparable long-term stability up to 10 weeks [60]. By covalently linking the enzyme with the BSA by means of glutaraldehyde molecules, a matrix is formed in which the natural conformation of the enzyme is preserved (Fig. 2.2).

To prepare the enzyme solution, the same steps described by Mross et al. were taken [23]: 10 mg glucose oxidase (activity 100 - 250 U/mg) or 10 mg lactate oxidase (activity 30 U/mg) were dissolved in 10 mg bovine serum albumin in 1 mL of 10 mM PBS. After thorough mixing, 50 μL of 8% glutaraldehyde (v/v) was added and the solution was mixed again. On WEs surfaces, 0.1 μL of the solution was dispensed using a microliter pipette and left to dry in air.

Then, the polyurethane membrane was prepared by dissolving PU pellets in concentration of 4% in a mixture of tetrahydrofuran and dimethylformamide solvents in a ratio THF:DMF of 5:5. In Mross et al. work [3], those values provided the most homogeneous membrane with the best trade-off between sensitivity and linear range

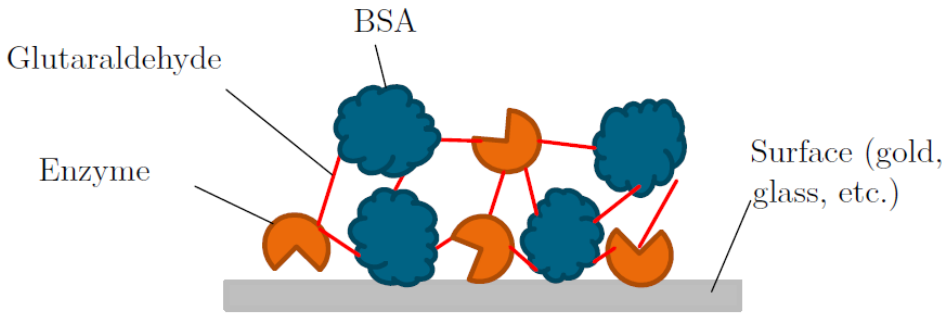

Figure 2.2: The crosslinked matrix of enzyme, bovine serum albumin (BSA) and glutaraldehyde on top of a surface.

extension. An amount of 0.15 μL of the solution was applied on the enzyme layer and dried in air.

Following these realization steps, the glucose sensor was supposed to exhibit a resolution of 5 mM and a sensitivity around 0.4 nA/mM, with a linear range up to 300 mM and a plateau maximum current of 150 nA [23]. This is consistent with the typical concentration ranges of glucose and lactate in bioprocesses of around 50 mM for mammalian cell cultures as discussed in Section 1.2.2.

At the same time, the response time should fit the characteristics of the monitored bioprocess, in order to monitor and control the analyte levels fast enough. Hence, taking as reference the doubling time of bacterial cells in a bioreactor as 20-30 min [1], a suitable enzyme sensor should have a response time below 20 min.

Concerning sensor calibration, glucose solutions of different concentrations were prepared in 10 mM PBS. Amperometric measurements were performed at room temperature (22°C) using a VersaSTAT 4 potentiostat (Ametek Scientific Instruments).

2.2 Cell Density Sensor

One way to determine the cell density is to calculate the conductivity values both at very low frequency and at very high frequency: as stated before, below

the characteristic frequency all cells are expected to contribute to the impedance, whereas above it there should be no influence of the cells anymore. Therefore, the conductivity ratio $\sigma_{high}/\sigma_{low}$ could be taken as a measure for the cell density. As a consequence, the f_{high} and f_{low} should be well-defined and extended values in such a way that the f_{char} is included in the ohmic plateau. Since in this ohmic plateau capacitive influences are avoided, changes in conductivity can be readily detected without any distortions.

The most suitable electrode structure for impedance spectroscopy measurements is the interdigitated electrodes (IDEs), which give the lowest impedance for the frequency range where the total impedance should be equal to the sensing element R_{sol} [39]. Hence, IDEs allow to derive the conductivity-frequency relationship using the so-called cell constant K_{cell} [61]. This parameter takes into account the number of fingers N, the finger length L, width W and spacing S and it is calculated as:

$$K_{cell} = \frac{2}{(N-1)L} \cdot \frac{K(k)}{K(\sqrt{1-k^2})} \tag{2.1}$$

$$K(k) = \int_0^1 \frac{1}{\sqrt{(1-t^2)(1-k^2t^2)}}\, dt \tag{2.2}$$

$$k = \cos\left(\frac{\pi}{2} \cdot \frac{W}{S+W}\right). \tag{2.3}$$

Relying upon Olthius et al. work [61], the R_{sol} and C_{elec} expressions can be derived for an IDE:

$$R_{sol} = \frac{K_{cell}}{\sigma_{sol}} \tag{2.4}$$

$$C_{elec} = \frac{\varepsilon_0 \varepsilon_{r,sol}}{K_{cell}} \tag{2.5}$$

with σ_{sol} and $\varepsilon_{r,sol}$ being respectively the solution conductivity and permittivity. Then, the double layer capacitance C_{DL} could be calculated as [39]:

$$C_{DL} = WLNC_0 \tag{2.6}$$

with $C_0 \approx 10\,\mu F/cm^2$. Thus, the aforementioned estimations of the cutoff frequencies can be rewritten as:

$$f_{low} \approx \frac{\sigma_{sol}}{\pi W L N C_0 K_{cell}} \tag{2.7}$$

$$f_{high} \approx \frac{\sigma_{sol}}{2\pi(\varepsilon_0 \varepsilon_{sol} + K_{cell} C_{wire})}. \tag{2.8}$$

Moreover, the f_{low} and K_{cell} expressions can be simplified by taking into consideration that the widest ohmic plateau has been found for a ratio $S/W = 0.54$ [62]:

$$k^* = \cos\left(\frac{\pi}{2}\frac{1}{1.54}\right) = \cos\left(\frac{\pi}{3.08}\right) = 0.523 \tag{2.9}$$

$$K(k^*) = 1.65 \qquad K\left(\sqrt{1-k^{*2}}\right) = 2.15 \tag{2.10}$$

$$K_{cell}(k^*) = \frac{1.53}{(N-1)L} \tag{2.11}$$

$$f_{low} = \frac{\sigma_{sol}}{0.48W} \cdot \frac{N-1}{N}. \tag{2.12}$$

Previous studies on yeast cultures showed that the characteristic frequencies are in the order of megahertz, e.g. around 14 MHz for E. coli cells, few MHz for S. cerevisiae cells [17]. In this work, electrodes were designed in different variants with an ohmic plateau extending to either f_{high}= 10 MHz or 20 MHz. The conductivity (σ_{sol}) and the permittivity ($\epsilon_{r,sol}$) of the cell medium were respectively assumed as 1 S/m [7] and 80 [3]. Moreover, an instrument wire length of 2 m was considered, giving a wiring capacitance of C_{wire} = 200 pF. Therefore, the cell constants in the two upper-limit frequency cases were calculated by rearrangement:

$$K_{cell} = \frac{\sigma_{sol}}{2\pi C_{wire} f_{high}} - \frac{\varepsilon_0 \varepsilon_{r,sol}}{C_{wire}} \tag{2.13}$$

$$K_{cell,\,10MHz} = 0.76\,cm^{-1} \tag{2.14}$$

$$K_{cell,\,20MHz} = 0.36\,cm^{-1} \tag{2.15}$$

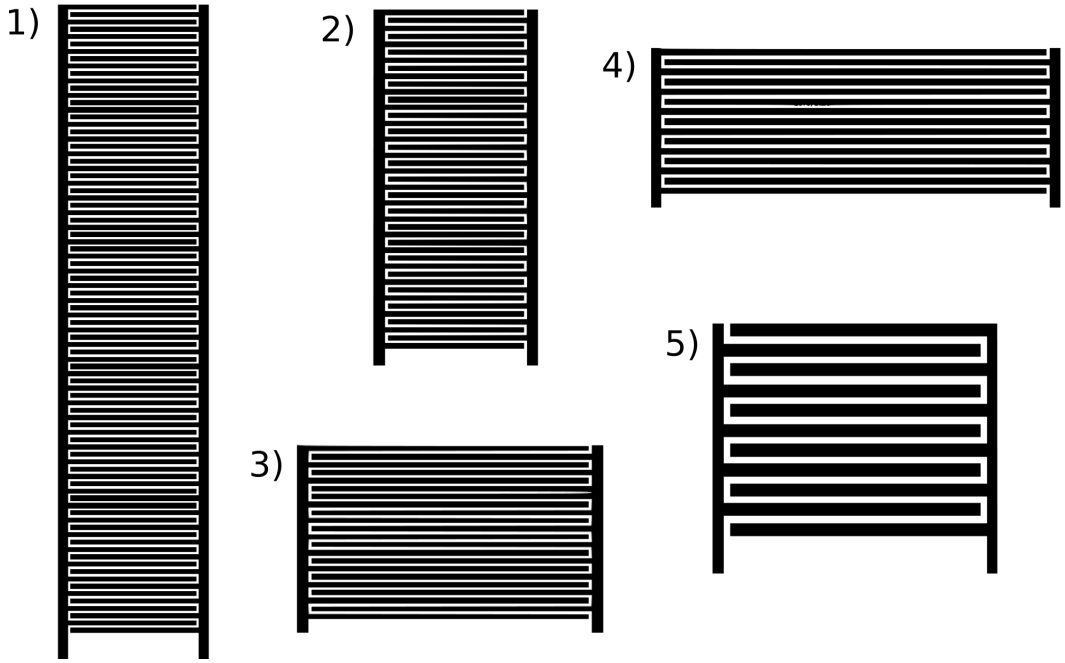

Figure 2.3: Design variants of interdigitated electrodes.

IDE design rested on Mross' work [22], where a minimum spacing S of 10 μm was chosen, as the smallest producible distance between structures using a lift-off procedure. This value didn't undermine the validity of the experiment, since yeast cells have a diameter between 2 μm and 10 μm [37], letting the detection of approximately two yeast cells in z-direction if cells were assumed to be directly adjacent to each other. Hence, a minimum width W of 18.5 μm was chosen, besides the values of 37 μm, 50 μm and 100 μm. The finger length L was arbitrary set to values between 100 μm and 3000 μm with corresponding numbers of fingers N, that was expressed as a function of K_{cell} and L. Five feasible variants were set up, as shown in Fig. 2.3 and listed in Tab. 2.1.

For calibration setup, the impedance spectra of the variants were evaluated in 10 mM PBS. Measurements were recorded by using yeast suspensions of increasing concentrations. Both the analysis were performed using a Bode 100 network analyzer (OMICRON Lab) with a two-port impedance probe. Then, the impedances and phase angles at 1 MHz and 10 MHz were measured, the conductivity values calculated and the relation $\sigma_{10MHz}/\sigma_{1MHz}$ taken as a measure for the cell density.

Var	f_{high} [MHz]	f_{low} [kHz]	R [Ω]	L [μm]	N	W [μm]
1	20	112	36	500	86	18.5
2	20	56.3	36	1000	43	37
3	20	56.3	36	2000	22	37
4	20	41.6	36	3000	15	50
5	10	20.8	76	2000	11	100

Table 2.1: Design variants of interdigitated electrodes with cutoff frequencies, resistance and design parameters finger length L, number of fingers N and finger width W.

2.3 pH Sensor

In this work, the working electrode surface was functionalized with a polyaniline coating. Polyaniline has been commonly used in past for pH sensing because of its reversible protonation/deprotonation reaction, high stability, low cost and easy preparation procedure [63, 64].

As shown in Fig. 2.4.a, polyaniline chains consist of amine and imine groups which can be reversely oxidized/reduced upon protonation/deprotonation [65]. In Fig. 2.4.b the reversible protonation process is shown. Among several techniques developed to prepare conducting polymer films, electrochemical deposition of polyaniline was preferred as it allows to cover only the exposed electrode surface and to control the thickness of the film by monitoring the total charge through the electrochemical cell during the functionalization process [66, 65]. The WEs surface is typically functionalized by electropolymerizing small droplets of aniline and HCl solution by means of cyclic voltammetry. A schematic representation of the potentiometric measurement is presented in Fig. 2.5.

In this work seven variants wer designed in order to study sensors response changing the electrode area: 500x500, 500x800, 500x1000, 500x1200, 300x1000, 400x1000, 400x1200 (dimensions in μm). The RE was made of silver with a silver-chloride layer galvanically plated. Gold was chosen for WE as conductive electrode material, since good results have been achieved in a recent work developed in the KU Leuven NanoCenter cleanroom [67]. Then, a solution of a 0.2 M aniline and 0.8 M HCl

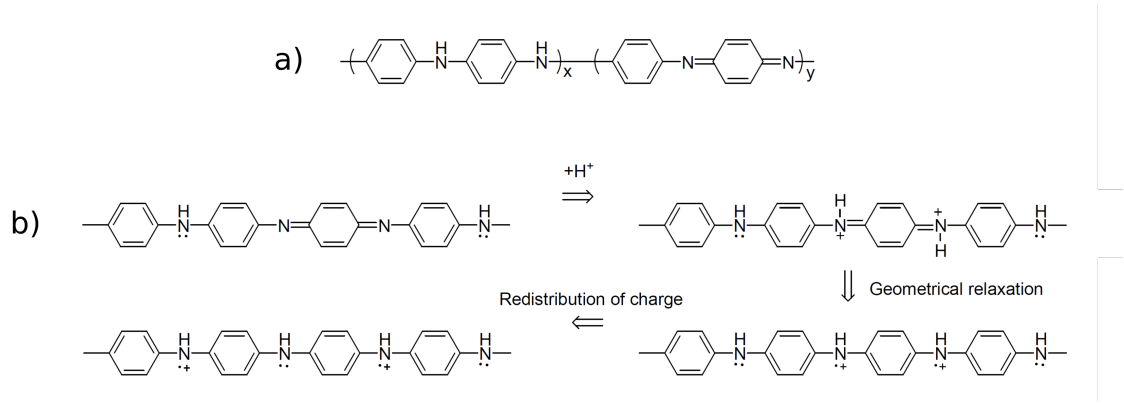

Figure 2.4: Structure (a) and protonation process (b) of polyaniline.

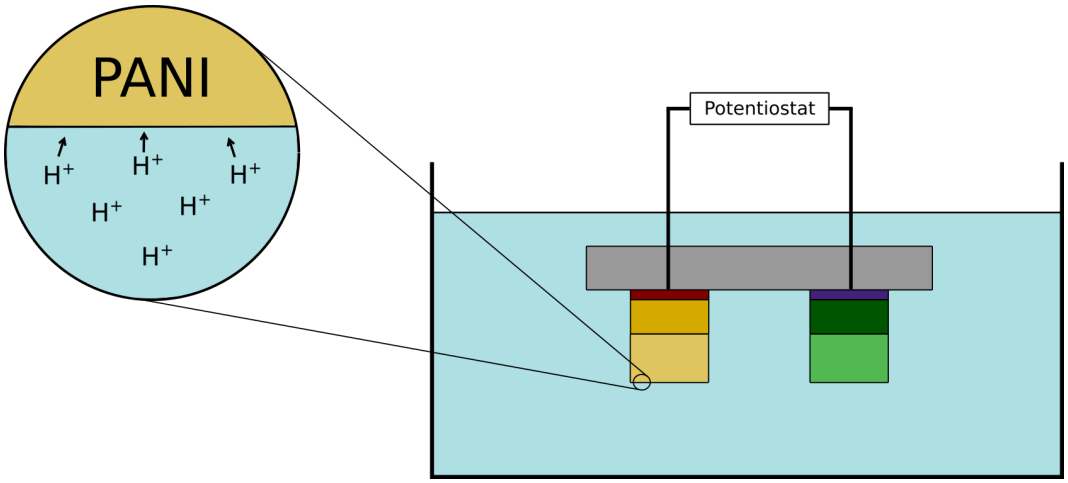

Figure 2.5: Schematic overview of the two-electrode electrochemical cell (WE on the left and RE on the right) with a detail of the H^+ ions sensing mechanism.

was electropolymerized on top of the WE surface by means of cyclic voltammetry (CV), using an external platinum electrode as counter electrode and a Ag/AgCl one as reference. The WEs of the various chips were all connected to a common gold square (1 cm x 0.7 cm) which was connected to a potentiostat (VersaSTAT 4, Ametek Scientific Instruments) by means of a crocodile clamp: in such a way, all the WEs of the pH sensor were functionalized at the same time with the same settings. The voltage was scanned 5 times between 0 and +1.5 V with respect to the Ag/AgCl RE, in order to passivize the electrode surface, ensuring a smooth deposition, and swept at a constant sweeping rate of 20 mV/s. As final step, substrates were rinsed

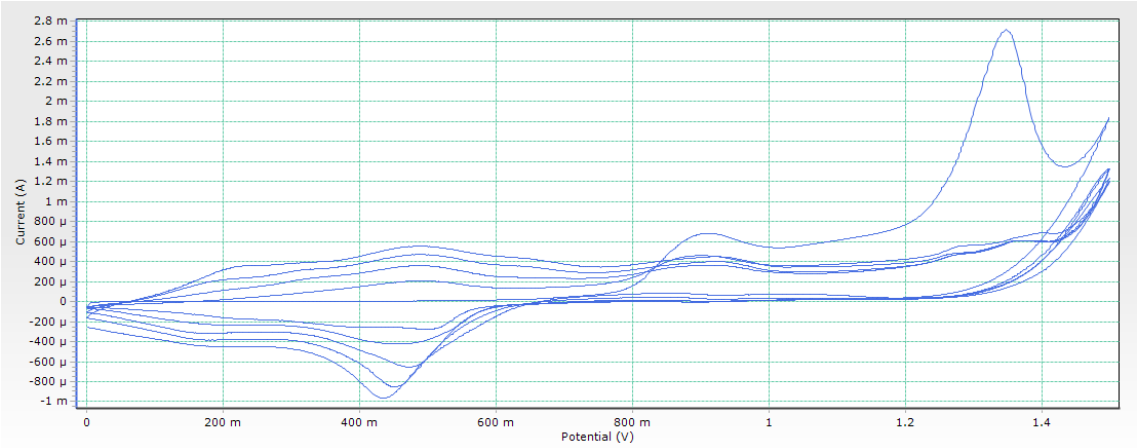

Figure 2.6: Obtained cyclic voltammogram of polyaniline electrodeposition on top of the gold working electrodes (picture acquired from VersaStudio software).

with deionized water and dried on a hot plate at 60° C for 5 minutes.

A picture of the cyclic voltammetry of the electropolymerization of aniline on top of the WE surface is depicted in Fig. 2.6. The voltammogram was consistent to those obtained in past works, with oxidation/reduction current peaks in correspondence of quite the same voltage values [68, 67].

The potentiometric response was measured as open circuit voltage (OCV) using a VersaSTAT 4 potentiostat (Ametek Scientific Instruments). The sensor was expected to perform a theoretical Nernstian behavior (-59.1 mV/pH), with an accuracy of 0.1 units which is considered an acceptable value to detect small variations of pH in cell cultures [18].

Ideally the electrochemical cell is modelled as high impedance, hence no net current should flow through the cell and an equilibrium potential is established [67]. For a better understanding of the potential drops involved during the potentiometric measurements, it's convenient to illustrate the electrochemical cell structure as follow [67]:

$$\underset{E_1}{\mathrm{Ag}} \,\big|\, \underset{E_2}{\mathrm{AgCl}} \,\big|\, \underset{E_M}{\mathrm{Sample}} \,\big|\, \underset{E_3}{\mathrm{Polyaniline}} \,\big|\, \mathrm{Au}$$

Referring to the formula (1.16), the measured open circuit potential response can

be described as the sum of the interfacing local potentials $E = (E_1 + E_2 + E_3) + E_M$. For a given temperature, E_1, E_2, E_3 can be considered constant and E_M is the only term dependent on the activity of the hydrogen ions in the solution, hence on pH. In this way, the open circuit potential response of the electrochemical cell as a function of pH is derived.

2.4 Dissolved Oxygen Sensor

In this work four variants were designed in two different configurations (Fig. 2.7). The decision of choosing several variants was based on studying sensors response changing UMEs diameter and number. UMEs diameters of 4 μm, 5 μm, 6 μm and 10 μm were chosen, with a surface area respectively of 680 μm x 680 μm, 300 μm x 1000 μm 660 μm x 660 μm, 400 μm x 1000 μm. Considering an inter-electrode distance of 10 times the value of the electrodes diameters, in order to have loosely packed arrays where the diffusion fields of the individual UMEs don't overlap [69, 70], variants of 256, 95, 100, 36 UMEs respectively were designed.

On the other hand, the concentric-electrodes configuration was compared to the parallel-electrodes one, in order to prove that the first one has a bigger current density than the other one. Indeed, it's intuitive to think that the current between WE and CE would have a bigger spreading field in the first case.

The reaction mechanism is based on the electrochemical reduction of the dissolved oxygen at the working electrode in a two-process step [7, 20, 71]:

$$O_2 + 2H^+ + 2e^- \longrightarrow H_2O_2 \tag{2.16}$$

Meanwhile, the oxidation reaction occurs at the counter electrode:

$$2H_2O_2 \longrightarrow O_2 + 4H^+ + 4\,e^- \tag{2.17}$$

Hence, the overall reaction is a 4-electron transfer process.

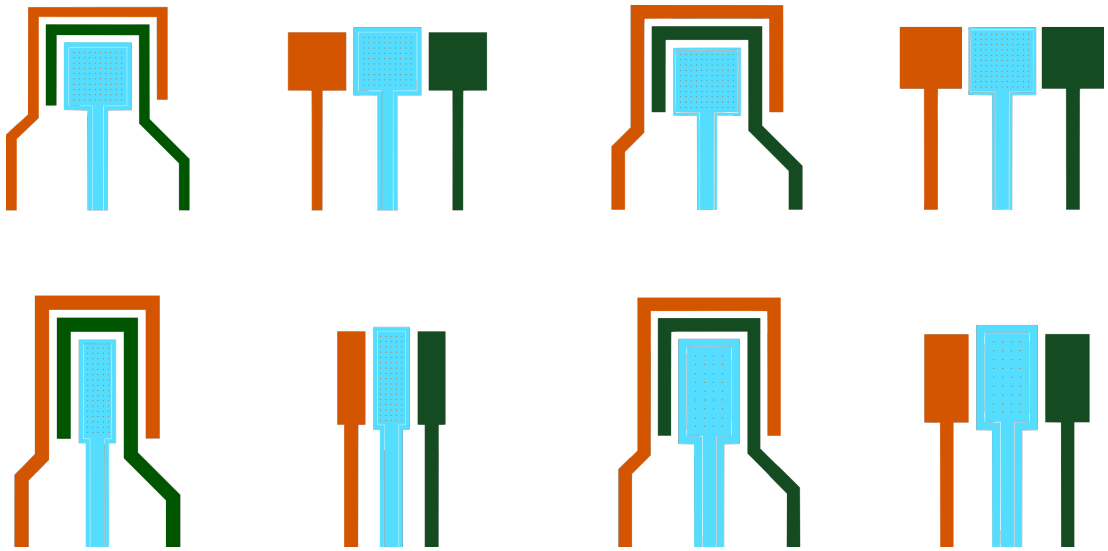

Figure 2.7: Design of the oxygen sensor variants; the electrodes in orange are the CEs, in green the REs, in light blue the WEs.

Depending on the application, the oxygen concentration is expressed either in relative numbers (e.g., percent saturation, volume percent, percent oxygen, ppm) or in absolute numbers (e.g., mg/L, mmol/L) [48]. Dissolved oxygen levels in culture media displayed substantial variability ranging from 6 – 11 mg/L (10% O_2 - 21% O_2) in cell culture medias [72].

Consequently, the required sensitivities for oxygen sensors are in the order of few μA/ppm [73] or few nA/mg/L [7], depending on the density of the monitored solution ($mg/L = ppm \cdot density/1000$).

Amperometric measurements were performed, as for the glucose sensor, at room temperature (22°C) using a VersaSTAT 4 potentiostat (Ametek Scientific Instruments).

2.5 Temperature Sensor

The smartest way to design a thin-film RTD in order to save space is the meander-line structure. The DC value of R can be estimated from the number of squares of

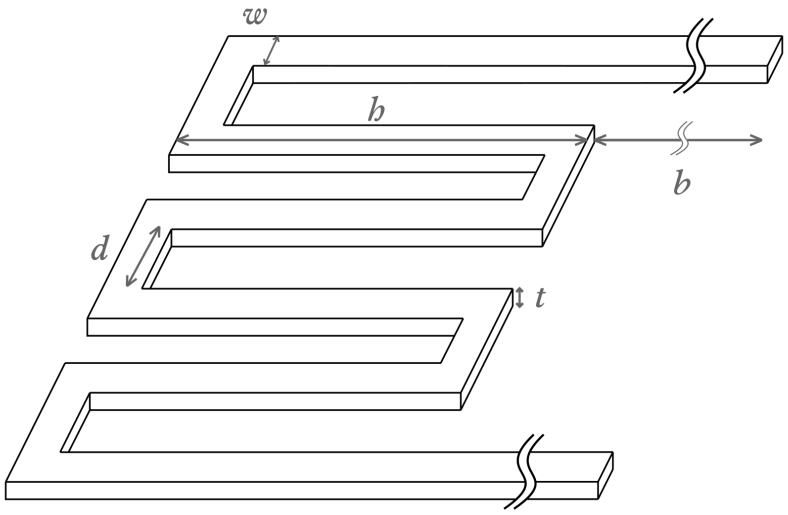

Figure 2.8: A 3D view of the meander-line resistor.

metal in the structure, neglecting the skin effect [74]. Thus, considering the design in Fig. 2.8, the series resistance is given by:

$$R = \rho \frac{L}{t\,w} = R_{sh} \frac{hN + d(N-1) + 2b}{w} \tag{2.18}$$

where $R_{sh} = \rho/t$ is the sheet resistance of the metal layer used for the resistor design and N is the number of line segments. In this work, the thickness t and the length b were fixed respectively to 200 nm, as the platinum layer height (neglecting the titanium adhesion layer of 20 nm), and 1.5 mm, as the distance from the chip active area and the chip edge (as will be discussed in Section 3.1). The other parameters, shown in Tab. 2.2, were chosen considering the different $R_{20°C}$ values and $\rho_{20°C}$:

$R_{20°C}$ [Ω]	b [μm]	w [μm]	d [μm]	h [μm]	N	L [μm]
100	1600	27	50	436	4	5094
500	1700	10	50	710	8	9434
1000	1700	5	50	710	8	9434

Table 2.2: Design variants of RTDs.

Taking $\rho_{20°C} = 1.06 \cdot 10^{-7}\,\Omega m$ as reference value [75], d, h, w and N were chosen in order to get $R_{20°C}$ equals to 100 Ω, 500 Ω and 1000 Ω. For the sake of simplicity,

these samples will be renamed as Pt 100, Pt 500 and Pt 1000 respectively, even if these definitions refer to RTD with a nominal resistance of 100, 500 and 1000 Ω at 0° C.

Temperature is one of the most critical variables to be monitored in order to grow cell cultures in a healthy environment. Therefore, temperature should be kept in the range 20° - 25° C, so to be suitable for growth of the majority of yeasts. An accuracy of ±0.5° C is typically considered adequate for cell culture monitoring [18].

Calibrations and measurements were conducted by varying temperatures and collecting data using a LCR meter (4284A Agilent) in a 2-wire configuration. The variants were dipped in a beaker filled with PBS which was heated upon a hotplate, whose temperature was monitored with a commercial type K thermocouple (AZ8852 K/J/T Thermometer).

Chapter 3

Sensor Integration, Fabrication and Measurement Setup

In this chapter the microfabrication techniques used for the chip implementation are explained. An overview of the overall processes, highlighting all the steps involved, and of the general measurement setup is given.

3.1 Sensor Integration

After designing the individual sensor elements, they were integrated on single multi-sensor chips that were designed using Cadence® Virtuoso Layout Suite software. The sensors were arranged in such a way that they didn't interfere with each other, therefore a minimum distance of 700 μm between each sensor was chosen. Considering also a distance of 1.5 mm between the chip active area and the chip edge for the epoxy layer protecting the bonding wires, a chip size of 7 mm x 7 mm was get.

A 3-inch glass wafer was used as substrate and this allowed to place 4 copies of 8 variants as shown in Fig. 3.1. Moreover, platinum and silver squares and circles were added respectively to test the dispensation of the enzyme solution and Nafion on top of the respective layers.

The arrangement was chosen in a way that allowed to place the bond pads on

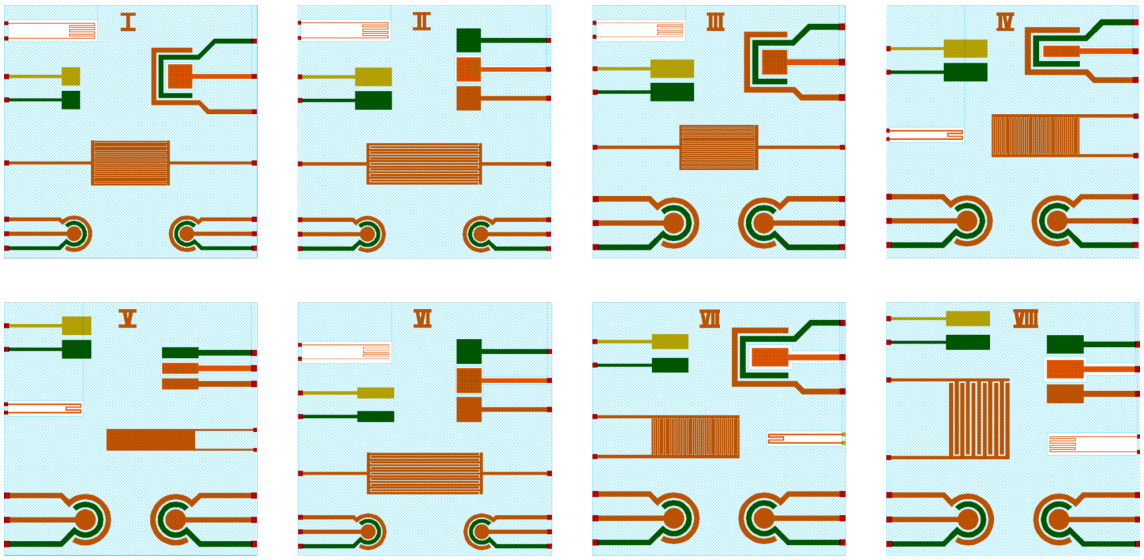

Figure 3.1: The 8 variants designed on Cadence Virtuoso Layout Suite software.

the left and right side of the chip, so that a dual in-line (DIL) package could be used for future integration of the multi-sensor chip. Since electrodes, isolation layers, leads and bond pads were produced from different materials, i.e., platinum, gold, aluminum, parylene-C, polyimide, the fabrication of these elements was carried out in four process steps.

The width of the leads connecting the sensor elements with the bond pads was chosen to give a low resistance but on the other hand to minimize the area for unspecific electrochemical reactions, which could distort the sensor signals. Hence, the maximum width was chosen as 140 μm, which gave a maximum resistance of around 10 Ω.

3.2 Chip Fabrication

The multi-sensor integrated chips were fabricated using standard microtechnology techniques in the cleanroom of the KU Leuven ESAT-MICAS department, housed in the NanoCentre (LeNa). All chemicals were purchased from Sigma-Aldrich (St. Louis, MO, USA).

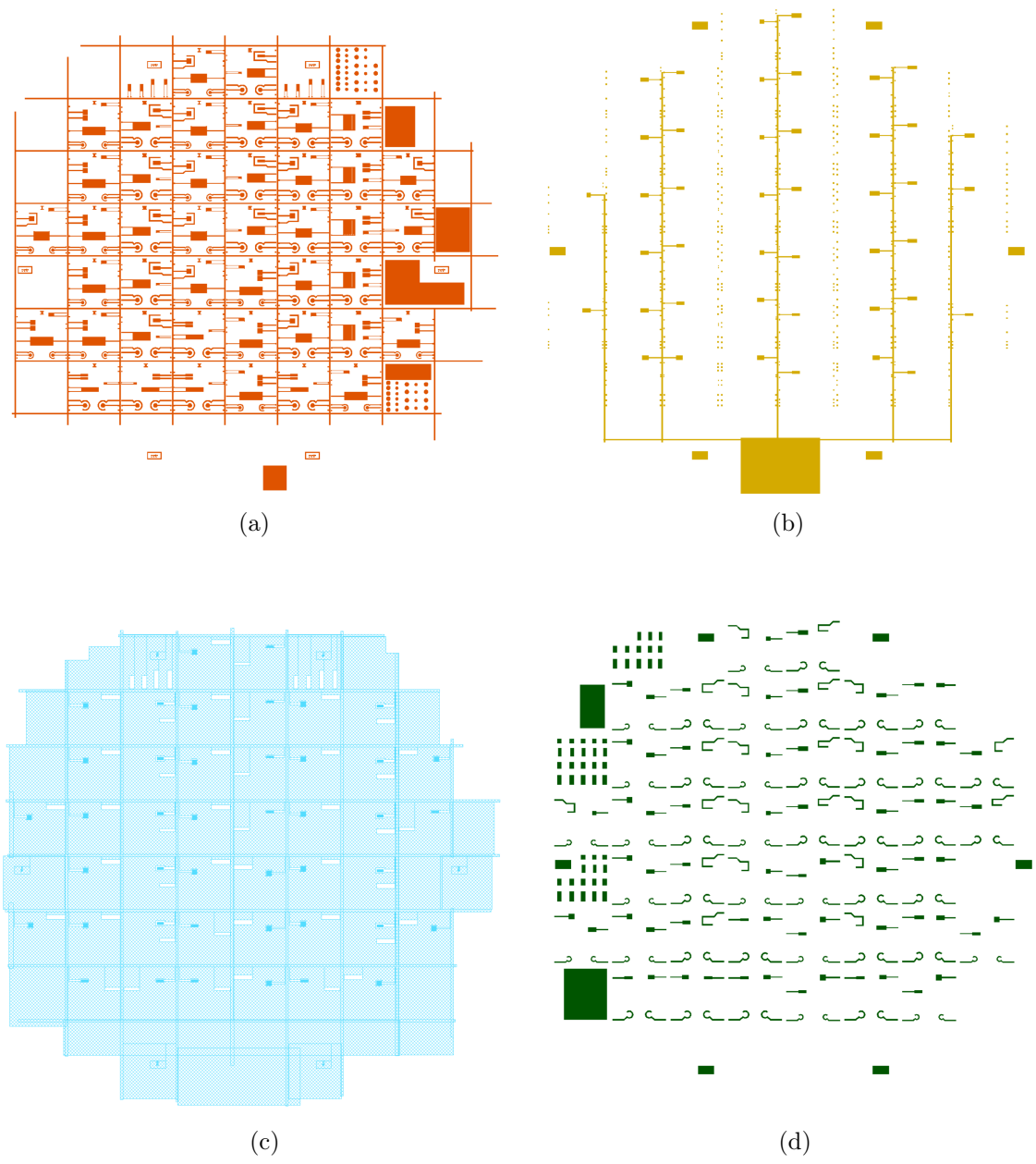

Figure 3.2: The four masks designed with Cadence® Virtuoso Layout Suite software: (a) platinum, (b) gold, (c) parylene-C/polyimide, (d) silver.

The layouts, shown in Fig. 3.2 and Fig. 3.3, were transferred to a photomask design using CleWin layout editor (WieWeb software) and four 4-inch masks (chromium on glass) were manufactured by using LW405 LaserWriter (MICROTECH).

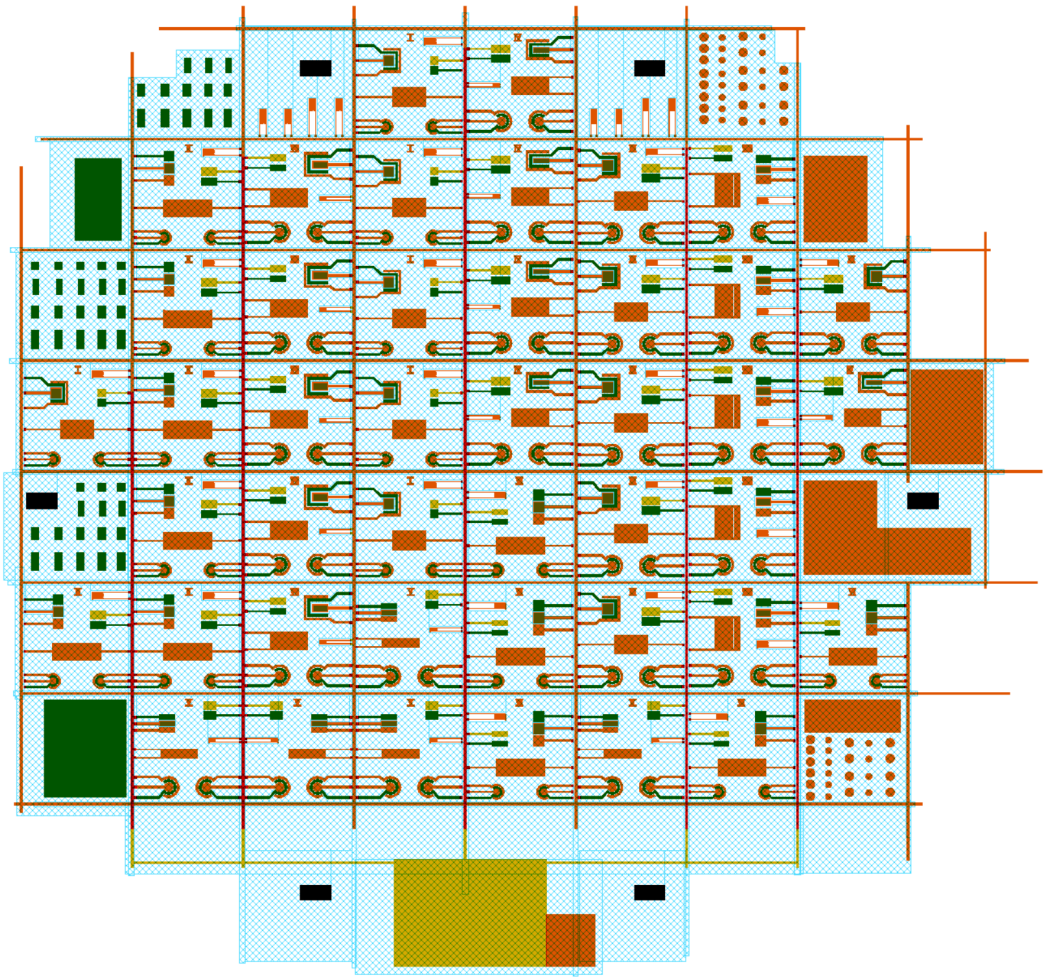

Figure 3.3: Overall layout of the four overlapped masks.

The electrodes were fabricated on four 700-μm thick 3-inch (75 mm $\pm$ 0.5 mm) Borofloat glass wafers. The fabrication process is schematically shown in Fig. 3.4.

As first step, the wafers were cleaned in acetone and isopropyl alcohol (IPA), rinsed in deionized water (DI) and put in ultrasonic bath for 5 minutes to remove any traces of contamination. Then, LOR10B lift-off photoresist (so to ensure discontinuous film deposition since it has a faster dissolution rate and dissolves isotropically) and S1818 positive photoresist were spin coated for 30 seconds individually at 3500 rpm and 4000 rpm and put on hot plates for 5 minutes at 180° C and for 2 minutes at 100° C respectively. The coated substrate was patterned using EVG®620 mask

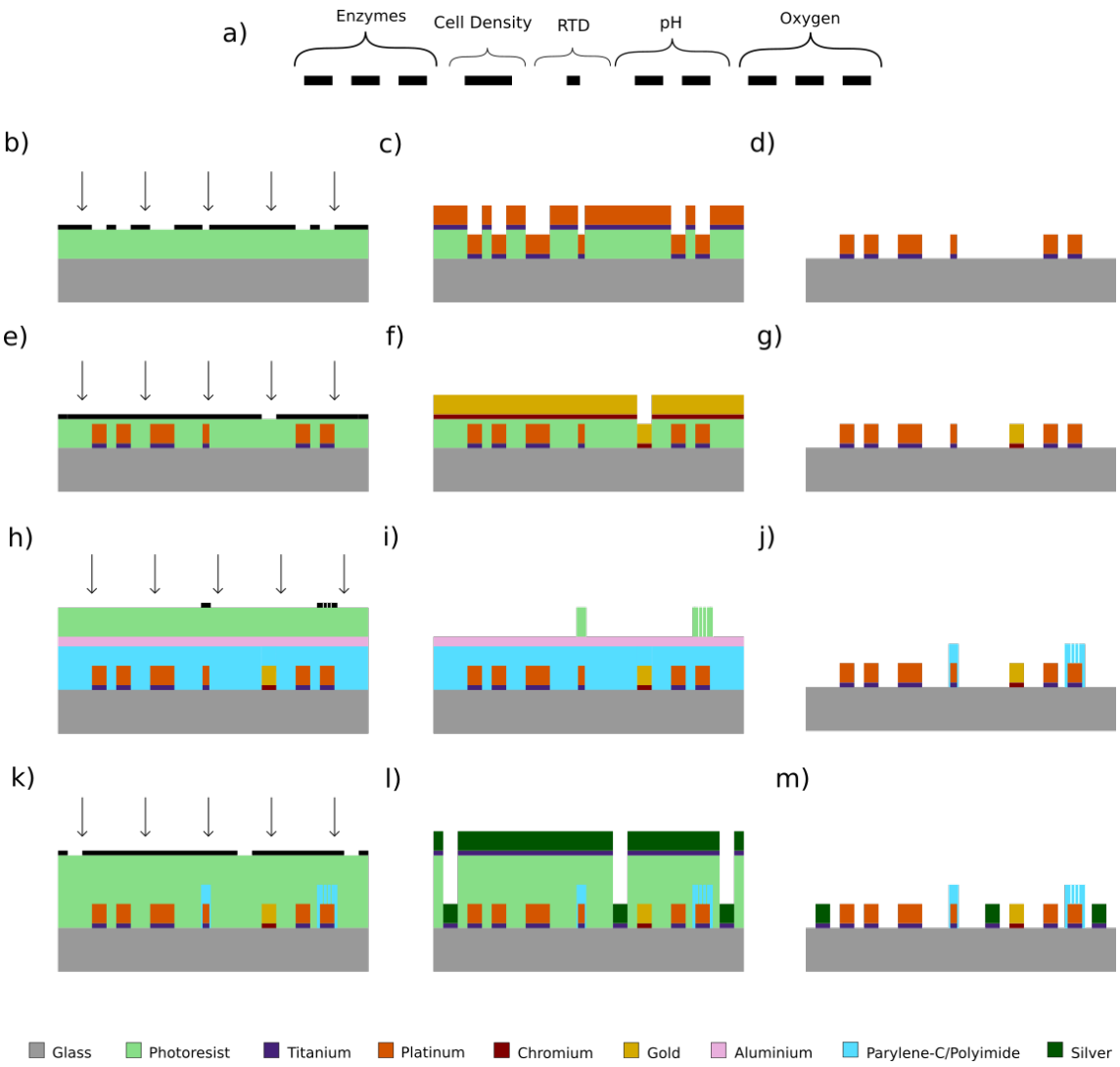

Figure 3.4: Flowchart of the chip fabrication steps.

aligner (25 mJ/cm^2, hard contact) and dipped in 351 (4:1) developer (Fig. 3.4.b).

Then, adopting Balzers BAE 370 sputter coater, 200 nm platinum on an adhesion layer of 20 nm titanium were sputtered for the working and counter electrodes of the enzymes and oxygen sensors, the interdigitated electrodes of the cell density sensor, the meander-line of the RTD and the first layer of the bond pads (Fig. 3.4.c). Afterwards, a lift-off process was performed by dipping the wafers in N-Methyl-2-pyrrolidone (NMP) solvent (Fig. 3.4.d).

For the working electrode of the pH sensor and for the second layer of the bond

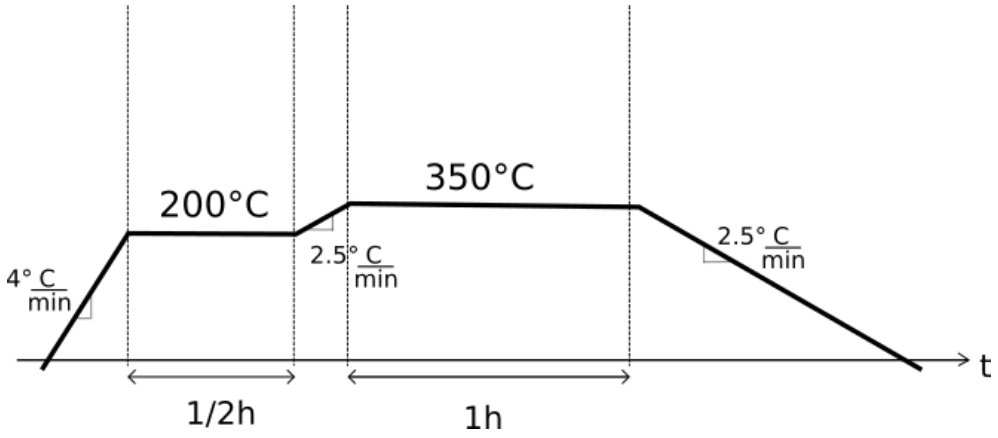

Figure 3.5: Graph of the polyimide baking procedure.

pads, LOR10B and S1818 photoresists were spin-coated, exposured and developed as previously described and 200 nm gold on an adhesion layer of 20 nm chromium were sputtered (Fig. 3.4.e-f). Subsequently, lift-off was performed using NMP (Fig. 3.4.g).

Concerning the working electrode of the oxygen sensor and the RTD, two isolation materials were used on different wafers due to problems with the machinery used. In particular, parylene-C was deposited on one wafer by chemical vapour deposition (CVD) using the Parylene coater PPCS, whereas on the other three wafers polyimide was spin-coated on top of an adhesion promoter layer and baked in oven with the procedure indicated in Fig. 3.5. Then, in both cases 100 nm aluminum was evaporated with Evaporator MED010 (Balzers Union) as hard-mask and both HMDS and S1818 were spin-coated and exposured to 25 mJ/cm^2 (Fig. 3.4.h). The wafers were dipped first of all in 351 (3:1) developer and afterwards in aluminum etchant (Fig. 3.4.i). Finally, the insulating materials and the photoresist layer were etched using reactive ion etching (RIE) procedure by using JLS etcher and the remaining aluminum layer was finally removed by the aluminum etchant (Fig. 3.4.j).

For the reference electrodes of enzymes, oxygen and pH sensor, LOR10B and S1818 photoresists were spin-coated, exposured and developed as previously described, 200 nm silver on an adhesion layer of 20 nm titanium were sputtered and lift-off was performed using NMP (Fig. 3.4.k-l-m). The AgCl layer was formed by applying a droplet of 50 μL 50 mM $FeCl_3$ (Iron(III) chloride, $\geq$99.99%) on top of

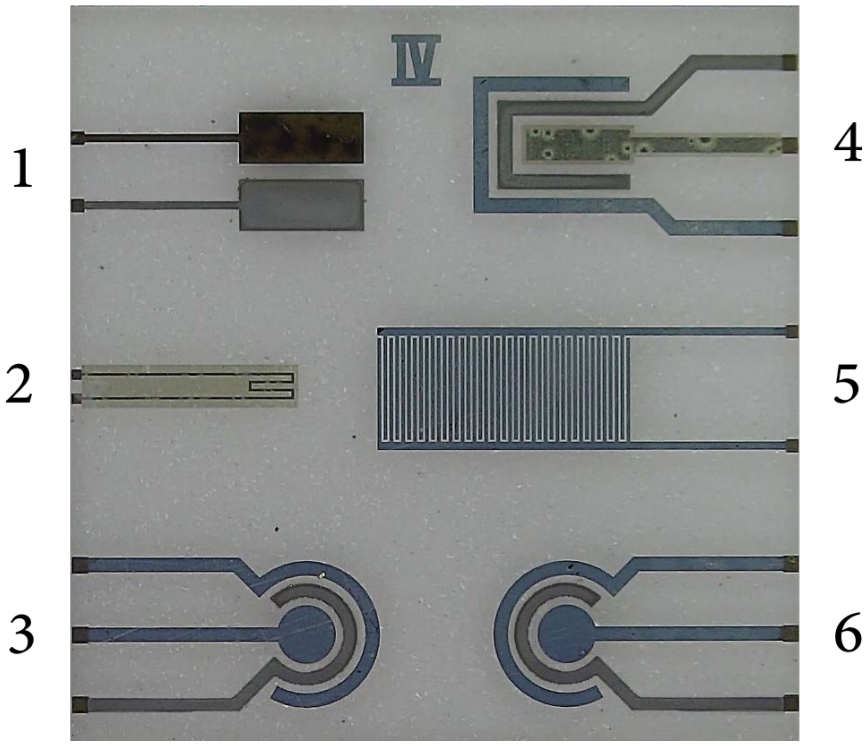

Figure 3.6: Picture of an implemented chip: (1) pH, (2) temperature, (3) glucose, (4) oxygen, (5) cell density and (6) lactate sensors.

the silver layer for 50 seconds in order to partially oxidize the silver layer to silver chloride. Electrodes were rinsed with DI, dried on a hot plate at 60° C for 5 minutes and stored in a saturated KCl solution for 2 hours to saturate the AgCl layer with Cl^- ions and rinsed with DI afterwards. Finally, a 3 μL droplet of 5wt.% Nafion perfluorocarbon resin solution dissolved 1:1 in N,N'-dimethyl formamide was applied on top of the formed Ag/AgCl layers using a capillary micropipet and placed on a hot plate at 60° C for 5 minutes in order to evaporate the solvent.

As last steps, polyaniline was electrodeposited onto working electrode surface of the pH sensor as previously described in Section 2.3. Concerning the enzyme sensors, only the working electrode of the glucose sensor was functionalized with the enzyme layer and covered by polyurethane (as depicted in Section 2.1), due to lack of time and redundance of the two processes. After production, the wafer was diced into individual chips using a back-end dicing saw.

A photograph of a fabricated chip is shown in Fig. 3.6.

3.3 Measurement Setup

In order to conduct in-situ measurements, the chip was mounted on one end of an elongated printed circuit board (PCB) and directly immersed into the proper solution. Electrical connections between the chip electrodes and the PCB pads were made by wire bonding and were protected by an epoxy isolating layer together with the chip edges. Furthermore a 24-pin header was manually soldered on the PCB, in order to connect the sensors electrodes to the external instrumentation by means of male-to-female jumping wires. A picture of the PCB is depicted in Fig. 3.7a.

Adhesion problems of silver were observed in wafers where polyimide was used as isolation layer, probably due to presence of residual contaminations coming from polyimide post-etching. Therefore, it was not possible to use the integrated reference electrodes and in all amperometric and potentiometric measurements an external saturated Ag/AgCl reference electrode was adopted.

Moreover, since the wire bonding of some integrated counter electrodes failed, an external platinum counter electrode was utilized in all the amperometric measurements in order to keep the same setup for every experiment.

For the amperometric measurements, hence for testing the glucose and oxygen sensors, VersaSTAT 4 potentiostat (Ametek Scientific Instruments) and external Ag/AgCl reference and platinum counter electrodes were used (Fig. 3.7b). The same setup was adopted for the potentiometric measurements, i.e. for the pH sensor, but without the counter electrode, since it was an open circuit voltage analysis (as described in Section 2.3). Concerning impedance spectroscopy, the operating principle of the cell density sensor was evaluated by connecting it to Bode 100 network analyzer (OMICRON Lab) with a two-port impedance probe (Fig. 3.7c). Finally, the resistance changes of the RTD were evaluated by means of 4284A LCR meter (Agilent) (Fig. 3.7d).

The different setups of the amperometric, impedance spectroscopy and impedance analyzing measurements are shown in Fig. 3.7.

(a)

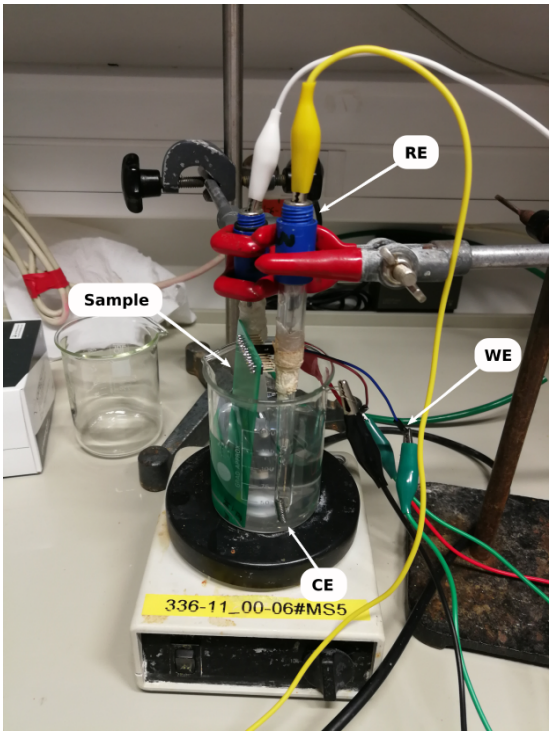

(b)

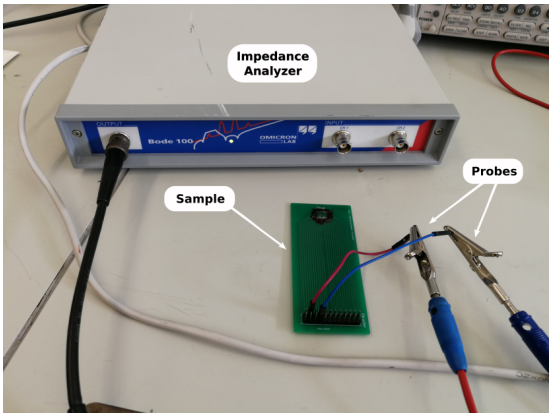

(c)

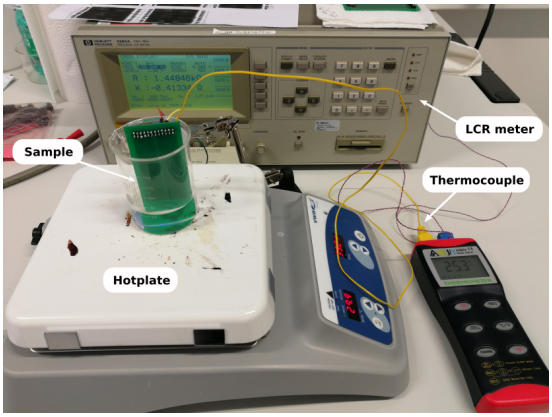

(d)

Figure 3.7: Pictures of (a) the chip mounted on the PCB board with the epoxy protective layer in black and the header at the bottom; (b) an amperometric measurement setup with the sample WE, external saturated Ag/AgCl RE and platinum CE connected to the potentiostat; (c) impedance spectroscopy measurements with the impedance analyzer setup; (d) LCR meter attached to the sample dipped in PBS which was heated upon a hotplate and whose temperature was monitored by means of a thermocouple.

The yeast used in all experiments was instant active dry yeast from Hambleton Bard Ltd., UK. It was suspended in 40° C water with brewing sugar in different concentrations (from 10 g/L up to 70 g/L) and let it ferment in sterile brown light-blocking bottles in a controlled environment of 22° C.

Chapter 4

Results and Discussion

In this chapter the electrical characterization of the sensors, by extracting all the relevant parameters and their variability, is presented, along with measurements which were performed by monitoring yeast cultures.

4.1 Glucose Sensor

Two variants with the same WE diameter of 566 μm but with different functionalization procedure were studied: the platinum surface of both the working electrodes was functionalized with glucose oxidase, but only one of them was covered with the polyurethane (PU) membrane. The reason of this choice was to investigate the response of the sensor in the two cases; specifically, the variant with the PU membrane was expected to give a wider linear range, as demonstrated in Section 1.2.2.

The characterization of the glucose sensor started with the performance of cyclic voltammetry (CV) measurements in 10 mM PBS solution using VersaSTAT 4 potentiostat (Ametek Scientific Instruments) with external platinum counter electrode (CE) and saturated Ag/AgCl reference electrode (RE). Prior to any amperometric measurements, this kind of analysis is always the first step to be made to determine the proper polarization voltage between the working electrode and the reference one. Indeed, for the amperometry setup the user has to set this parameter as the potential at which either oxidation or reduction reaction of the studied species exhibits.

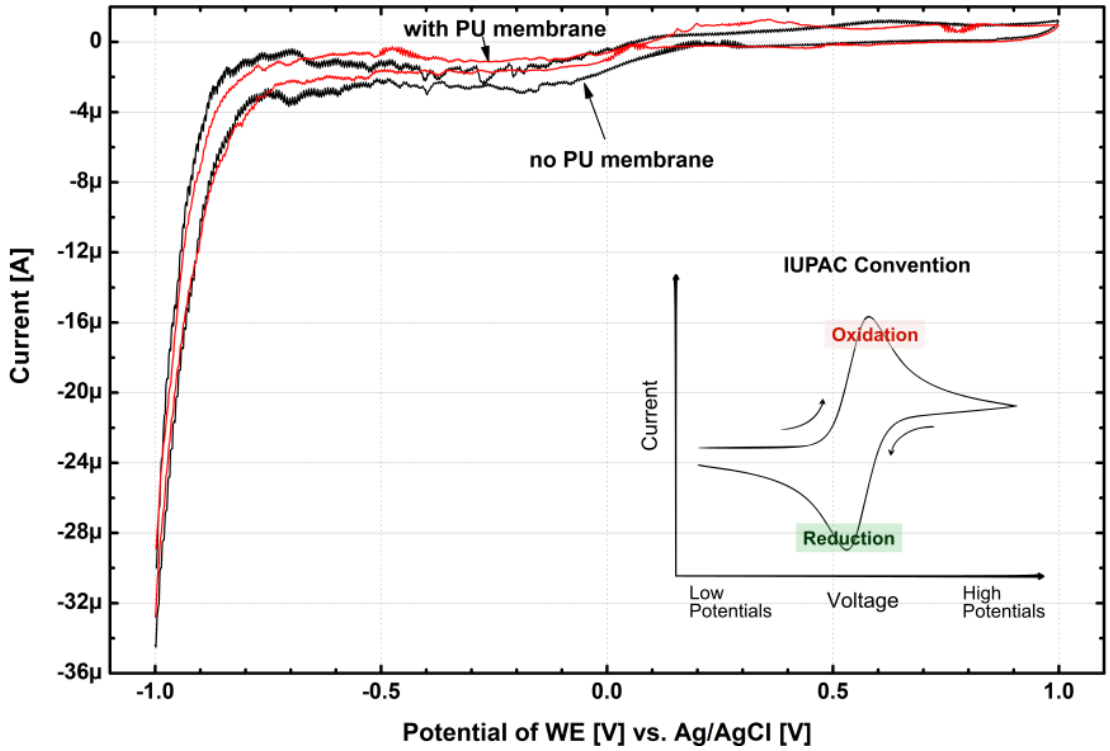

Figure 4.1: Determination of the polarization potential for the oxidation of H_2O_2 using cyclic voltammetry (CV) recorded using variants with the same (566 μm diameter) working electrodes whose surface was functionalized with glucose oxidase, but only one of them was covered with the polyurethane (PU) membrane. Inset shows the IUPAC convention for CVs.

As a matter of fact, the maximum selectivity at the maximum sensitivity is obtained [7, 76].

In this case, after running 5 cycles of CV with a scan rate of 100 mV/s in the voltage range [-1 V; 1 V] with respect to the Ag/AgCl RE, the oxidation of hydrogen peroxide (H_2O_2) was investigated, as explained in Section 1.2. Considering the IUPAC convention as depicted in Fig. 4.1, the figure shows that H_2O_2 oxidation took place in a potential range between 0.5 V and 0.9 V vs. Ag/AgCl RE. Within this range, a potential of 0.7 V was chosen as step voltage between the two electrodes for amperometric measurements, since at that potential it has been shown in literature that the measured current is specific for H_2O_2 oxidation [23].

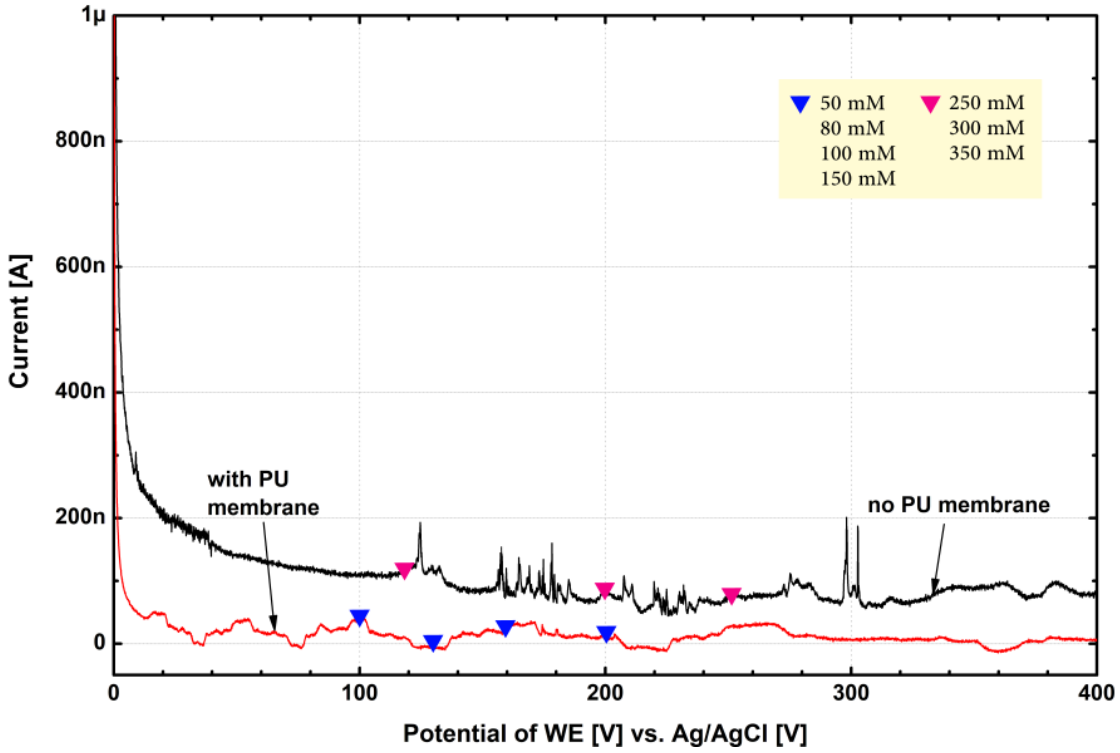

Figure 4.2: Response curve of the two glucose sensor variants after adding different concentrations of glucose (yellow box).

In order to calibrate the sensors, glucose solutions were prepared in PBS in different concentrations. The measurements were conducted for both the samples using different setups as visible in Fig. 4.2. Unfortunately, the both the sensors did not react to glucose changes. Indeed, the expected response would have been a slowly (up to 200 seconds) increase of the current until it reached a steady state value. Whereas in this case, no reaction was recorded from the electrodes. A magnetic stirrer was also used to mix the solution and dissolve properly the glucose powder, but it just resulted to add noise to the signal, which, anyway, was not affected by the various concentrations.

The only explanation to these results was the not proper functionalization procedure, since several sensors were tested and all of them gave the same responses. Apparently, inaccuracies in chemicals combination were made during the glucose oxidase layer compounding. The most likely hypothesis was the wrong unbalance

of the compounds, probably due to the low accuracy of the instruments, since very low quantities were employed.

The only positive aspect was that in the case of WE covered with the PU membrane the signal was lower as expected, since the flux of analyte molecules to the enzyme is reduced [23]

4.2 Cell Density Sensor

Impedance spectroscopy measurements were conducted by evaluating the fabricated interdigitated electrodes first in 10 mM PBS solution in a frequency range from 1 kHz to 40 MHz and then in yeast suspensions of increasing concentrations determined. Measurements were performed using Bode 100 network analyzer (OMICRON Lab) with a two-port impedance probe.

Due to time constraints, the performance of only two samples was investigated: variants number 2 and 5 (from Tab. 2.1) were chosen, because they differed significantly in finger width, spacing and length.

In order to estimate the cell density in yeast suspensions, the initial idea was to derive the conductivities from the impedances values at 1 MHz and 10 MHz; hence, the relation $\sigma_{10MHz}/\sigma_{1MHz}$ would have been derived and taken as a measure for the cell density, as explained in 2.2.

In this study, this was not possible since, as visible from Fig. 4.3, the spectra were compromised at frequencies higher than 1 MHz, due to a parasitic LCR load added by the passive probe. Indeed, this was confirmed by the fact that the first resonance peak was resistive-dependent (the lower the resistance value, the higher the peak), whereas the second one had the same behavior for each spectrum.

Hence, it was decided to directly take the impedance values in the middle of each plateau as a measure for the cell density.

A first characterization analysis was conducted by comparing the two variants in the same 10 mM PBS solution. The results are shown in Fig. 4.3 and listed in Tab. 4.1.

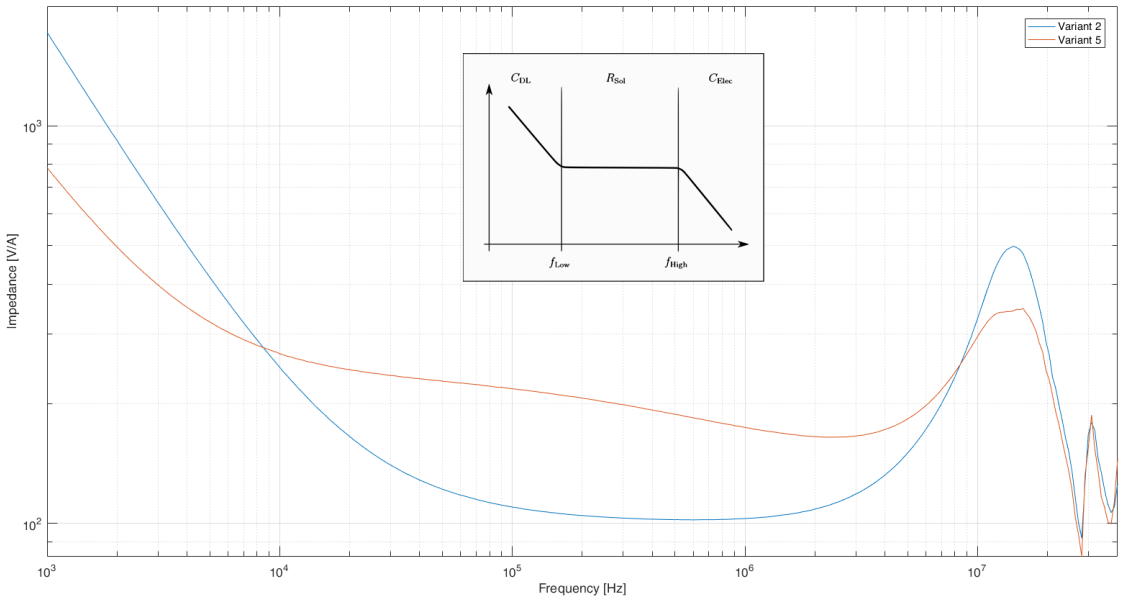

Figure 4.3: Impedance spectra of variant 2 and 5 in 10 mM PBS solution; inset shows the ideal spectrum of the modeled interdigitated electrodes.

Var	S [μm]	f_{low} [kHz]	$\hat{f}_{low}$ [kHz]	R [Ω]	$\hat{R}$ [Ω]
2	20	56.3	20	36	104.7
5	54	20.8	8	76	206.5

Table 4.1: Results of the impedance measurements in PBS solution for the designed variants with finger spacing S. Comparison between the calculated values of lower cutoff frequency f_{low} and resistance of the ohmic plateau R and the measured ones $\hat{f}_{low}$ and $\hat{R}$.

The lower cutoff frequencies were 64% and 62% lower than the values calculated in the design phase respectively for variant 2 and 5. This behavior was ascribed to a wrong estimation of either K_{cell}, C_0 or σ_{sol}, as derived in Eq. 2.7.

These results were in accordance also with the resistance values of the ohmic plateau: specifically, they were 65% and 63% higher than the expected ones respectively for variant 2 and 5. Indeed, the resistance was directly proportional to K_{cell} and inversely to σ_{sol} (Eq. 2.4).

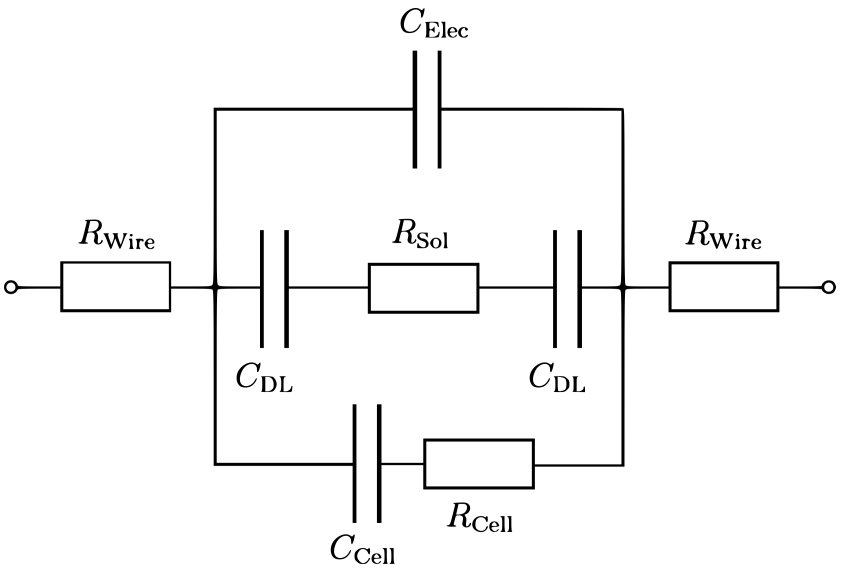

Figure 4.4: Equivalent circuit diagram of the sensor in contact with yeast cell suspension; C_{Cell}: capacitance of the cells, R_{Cell}: resistance of the cell membrane, C_{DL}: capacitance of electrical double layer, C_{elec}: capacitance between electrodes, R_{sol}: solution resistance, R_{wire}: wiring resistance.

Finally, considering correct the estimation of the conductivity, the calculation of the cell constant was assumed to be the main source of error. Such deviations of the cell constant have been reported in previous works and were ascribed to fringing effects at the substrate-solution interface, causing a deviation of the electric field lines [3, 77, 61].

Nevertheless, a clear relationship between the measured resistance and finger spacing could be established. In fact, the variant with the highest gap between fingers resulted to give the highest resistance value in the ohmic plateau, as expected [3].

Subsequently, calibration measurements in yeast suspensions with concentration of 10, 20, 30, 50 and 70 g/L were performed to evaluate possible impacts on the sensor performance. For these experiments, the equivalent circuit diagram in Fig. 4.4 was taken as reference, where the yeast cells were modeled as a capacitance C_{Cell} and a resistance R_{Cell}, thought to act in parallel. The calibration spectra of variant 2 are shown exemplarily in Fig. 4.5.

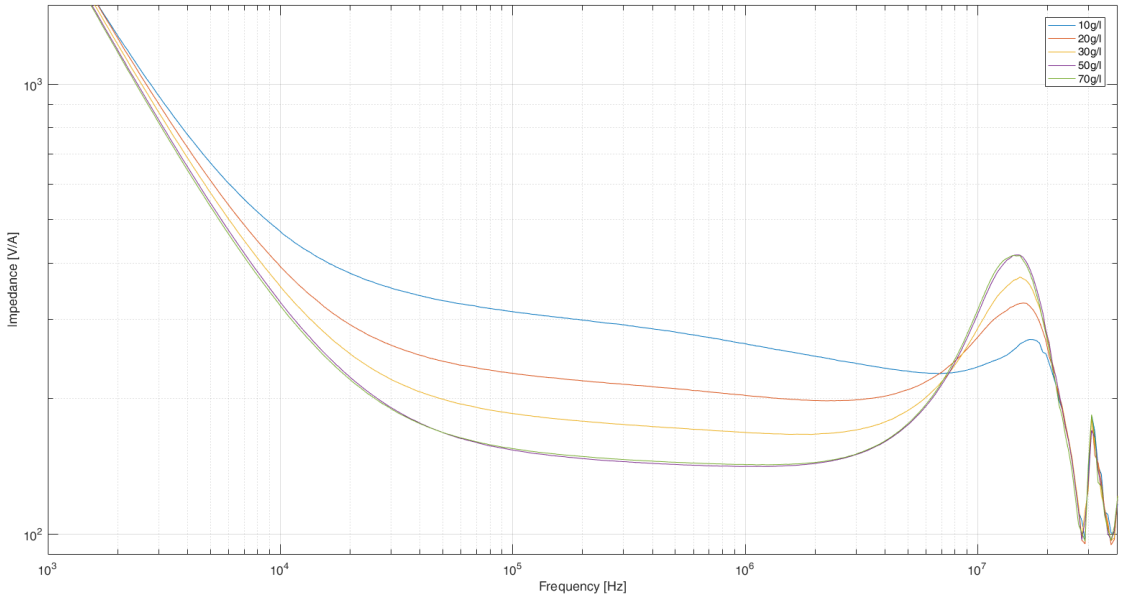

Figure 4.5: Impedance spectra of variant 2 in yeast suspensions of increasing concentration from 10 up to 70 g/L.

A clear dependence of the interdigitated electrodes response from the yeast concentration was observed. In fact, with increasing the concentration, hence the conductivity, the resistive impedance regime shifted to lower magnitude [77, 78, 79]. An explanation for the observed performance could be that solutions with higher cells concentration have higher levels of waste products, causing an increase of the salts dissolved in the electrolyte, hence of its conductivity.

Nevertheless, a further shift of the cut-off frequencies to higher values was not evident as expected. It is worth noting that in the measurement setup some drops of the prepared yeast solutions were dispensed on top of the chip and measures were taken right after waiting few minutes for the instrument to settle. Although the yeast cells were already grown and dissolved in the solutions, probably they did not sediment completely onto the chip surface. Apparently if the settlement time window had been extended, results more comparable to those expected would have been obtained.

An overview of the curve trend of the resistance at the middle of the ohmic plateau as a function of the cell density is depicted in Fig. 4.6. The non-linear

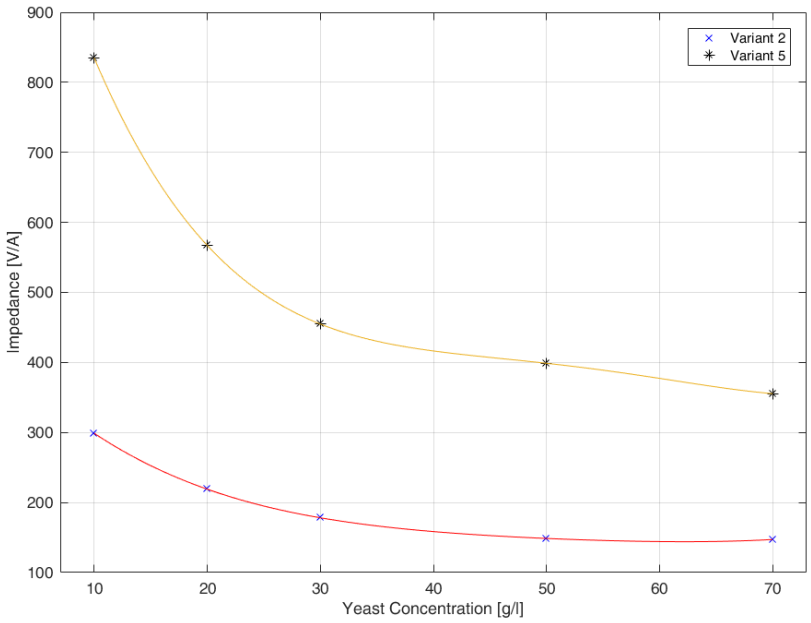

Figure 4.6: Calibration curves of the resistance at the middle of the ohmic plateau as a function of the cell density for the two variants.

dependence was reported also in previous works when dealing with high cell concentrations [3]. The very close similarity between the resistance values for 50 g/L and 70 g/L concentrations for variant 2 stands out. This was attributed to either a detection limit for this particular design or the non-verified repeatibility of the measurements that were carried out only once for each variant.

Once again, the relationship between the measured resistance and finger spacing was confirmed. In fact, the variant 2 with the highest gap resulted to give the higher resistance values than variant 5. Moreover, in the first case the sensitivity turned out to be higher, as proved in literature [3]. The explanation lies on the fact that electric fields of electrodes with narrower spacing are not able to reach farther into the cell solution, hence encountering more cells.

An outlook for future is to monitor the response of the interdigitated electrodes in parallel with a conductivity meters. In this way, higher accuracy and precision in measurements would be obtained.

4.3 pH Sensor

In order to calibrate the pH sensor as accurately as possible, the general procedure is to use standardized buffer solutions, whose ranges of measurement are known, and take at least two known data points to adjust the pH values associated with the voltage output [80]. In this work, buffer solutions of pH 4.0, 7.0, 10.0 (at 25° C) were used for the calibration procedure.

As mentioned in Section 2.3, open-circuit voltage (OCV) measurements were performed for 60 seconds using VersaSTAT 4 potentiostat (Ametek Scientific Instruments) and an external saturated Ag/AgCl reference electrode. During the performance of these measures, the room temperature was kept stable at 22.5° C. Due to time constraints, the performance of only four samples of two different variants was investigated: working electrodes with $400\mu m \times 1200\mu m$ (0.48 mm^2) and $500\mu m \times 1200\mu m$ (0.6 mm^2) area were tested.

As visible in Fig. 4.7, in most cases the OCVs remained quite stable for 60 seconds. In order to provide an overview of the samples performance, the mean value and the standard deviation of the acquired data were calculated and shown in Fig. 4.8. Deviations from the mean value were observed to be particularly high in the case of measurements recorded with buffer solution of pH 10. This was considered as a clear indication that the upper limit of the detection range of the designed pH sensor was less than 10, as also confirmed by some works found in literature where polyaniline was used as electropolimerized polymer [42, 43].

As illustrated in Sec. 1.4.1, an ideal pH sensor should follow a Nernstian behavior, hence it should exhibit a sensitivity of -59.1 mV/pH. The graphs in Fig. 4.8 showed that only the samples number 2, 3 and 4 followed a linear near-Nernstian response with sensitivities respectively of -52.4 ± 0.96 mV/pH, -50.1 ± 1.8 mV/pH and -45.1 ± 3.7 mV/pH. Meanwhile, the sample number 1 showed a sensitivity of -38.3 with a regression coefficient of 4.0 mV/pH. As a result, since the value is definitely lower than (3/4) x (Nernstian slope) (e.g. -44.3 mV/pH), this behavior is considered as sub-Nernstian, i.e. a subcategory of non-Nernstian responses [81].

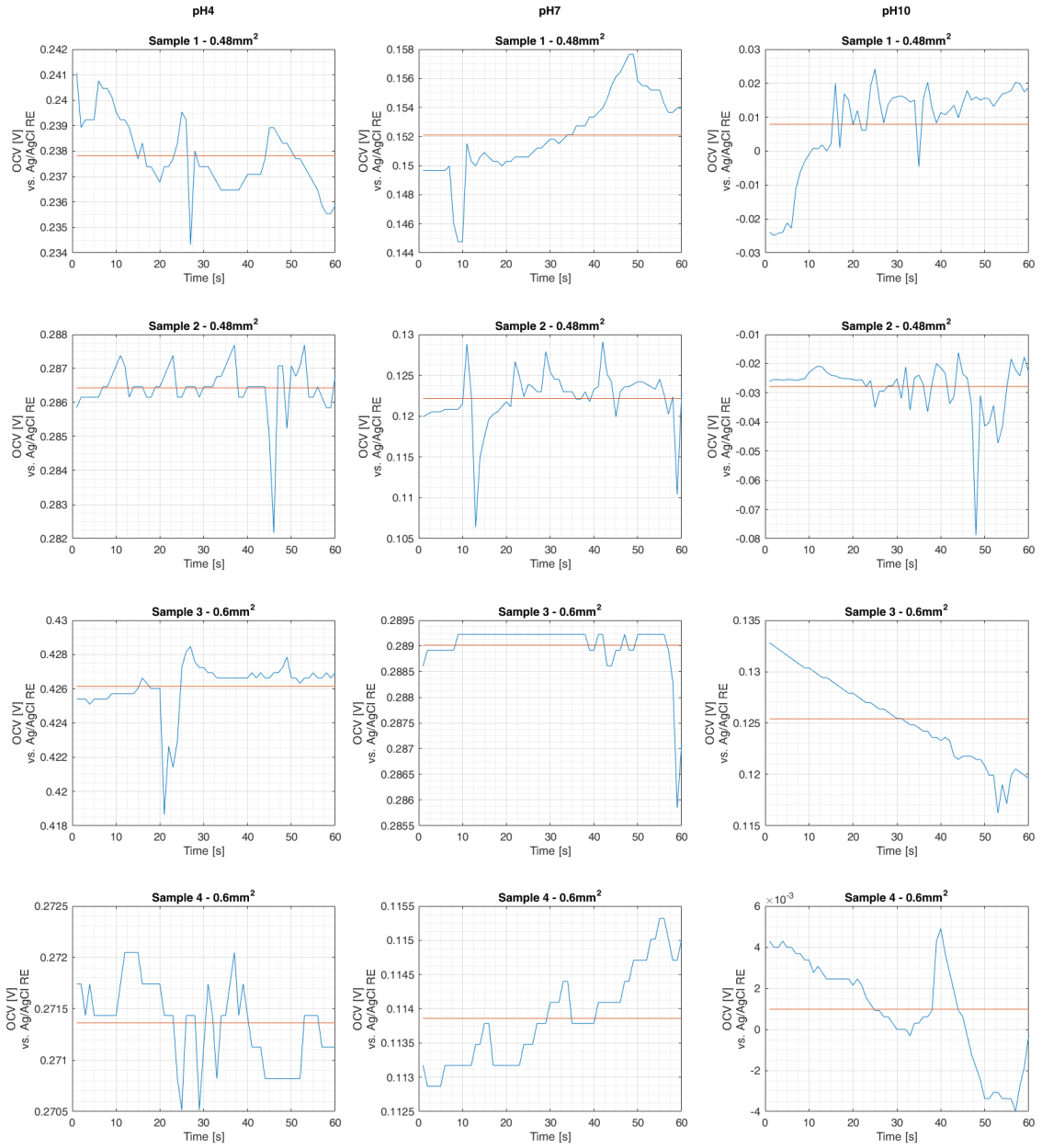

Figure 4.7: Evaluation of the open-circuit voltages (OCVs) with respect to the external saturated Ag/AgCl reference electrode (RE) in a time window of 60 seconds. Each sample (rows) was characterized by using standardized buffered solutions of pH 4.0, 7.0, 10.0 (columns). The blue line represents the monitored signal, while the red line the mean value of the data points.

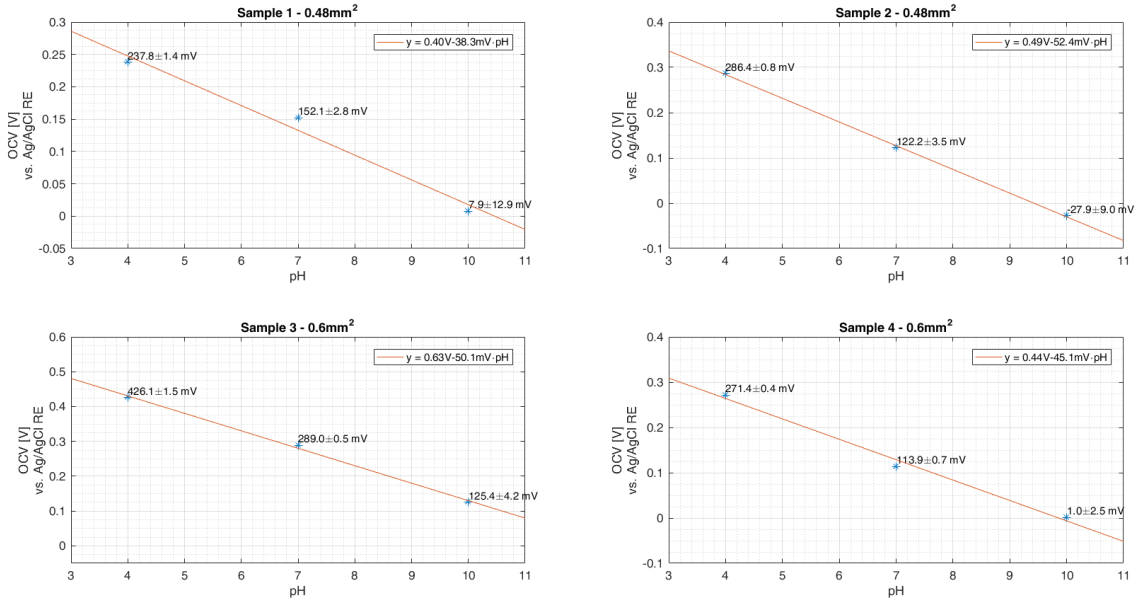

Figure 4.8: Open circuit voltage (OCV) response with respect to the external saturated Ag/AgCl reference electrode (RE) as a function of pH of the four samples. Regression lines (in red) expressions are derived (top right) from the mean values (blue asterisks) of the data acquired during the calibration setup.

In these cases, the local concentration polarization of the ions is partitioned at the sample/membrane interface between the two phases, due to ion-exchange or coextraction processes at the membrane interface. Therefore, this outcome could be ascribed to a non homogeneous deposition of the polyaniline layer on the working electrode surface.

In Fig. 4.8, the constant terms in the regression lines expressions of the four samples differed significantly from each other (487 ± 105.6 mV). Theoretically, considering the electrochemical cell structure illustrated in Section 2.3, if the potential between the solution and the reference electrode surface was supposed to be constant (since the same external saturated Ag/AgCl RE was used for all the measurements), it should mean that the only term changing among the samples is the potential between the polyaniline and the gold working electrode. This is probably due to a different distribution of the polyaniline layer on top of the metal surface. Hence, since all the working electrodes of each chip were electropolymerized at the same

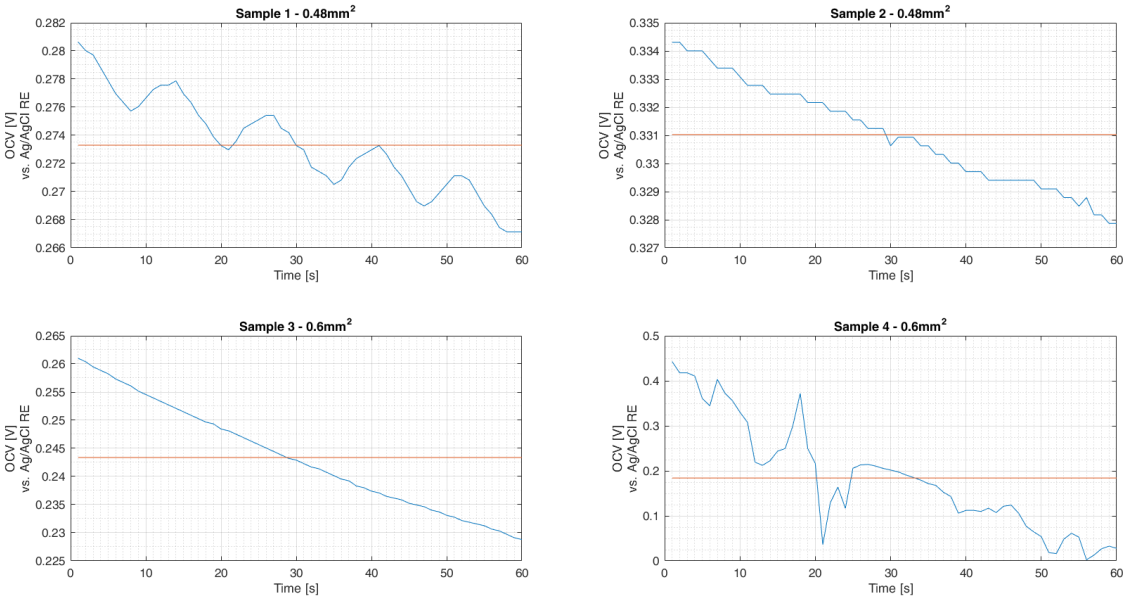

Figure 4.9: Evaluation of the open-circuit voltages (OCVs) with respect to the external saturated Ag/AgCl reference electrode (RE) in a time window of 60 seconds for each sample. The blue line represents the monitored signal, while the red line the mean value of the data points.

time with the wafers dipped in the same functionalizing solution, concentrations of aniline molecules were not probably the same at each trial.

Apparently, it seemed not to be any relationship between the working electrode area and the signal amplitude, as theoretically supposed, i.e. they should be related to a direct proportionality. This was attributed to the fact that the areas of the variants were quite similar to each other, as they differ of only 100 μm width. Moreover, sample number 3 gave higher values than expected: it looked like an offset was introduced, perhaps due to either wire bonding parasitisms or different polyaniline distribution during electrodeposition.

After calibration setups, measurements for pH detection were conducted by dipping the chip in a yeast solution with a concentration of 10 g/L. As evident from Fig. 4.9, all the samples showed a decreasing drift. For samples number 1, 2 and 3, the drifts were comparable, as clearly visible from Tab. 4.2, meanwhile sample number 4 performed very high drifting behavior.

Sample	OCV vs. time drift [mV/s]	pH vs. time drift [pH/s]	pH drift in 60s [pH]
1	-0.1850	$4.830 \cdot 10^{-3}$	0.29
2	-0.1045	$1.994 \cdot 10^{-3}$	0.12
3	-0.5394	$10.77 \cdot 10^{-3}$	0.65
4	-6.3422	$140.6 \cdot 10^{-3}$	8.43

Table 4.2: Comparison of the pH drifts for each sample during monitoring of yeast solution with a concentration of 10 g/L.

Unfortunately, there was not the possibility to monitor the pH of yeast solutions with a reliable commercial pH-meter (e.g., pH glass electrode or digital pH tester). Indeed, only in this way, conclusions on the actual functioning of the designed pH sensor could be drawn.

An outlook for future is to test the sensor response by using more standardized buffered solutions with a denser pH spectrum, in order to have more reliable sensitivities values and to determine the exact detection range. Additionally, the time window could be increased to higher values, so to have less signal drifts and variability.

4.4 Dissolved Oxygen Sensor

Prior to any amperometric measurements, a very effective tool used in characterization studies is the steady-state voltammetry (SSV). In this way, an estimate of the radius of the UME can be provided, as demonstration that the electrode response follows theory [55]. Typically well-studied aqueous systems having rapid electron transfer are used, including the oxidation of ferrocene methanol, the oxidation of ferrocyanide, the reduction of ruthenium hexamine and the reduction of ferricyanide. In SSV cycles conducted on UMEs the potential is swept slowly and triangularly, obtaining a sigmoidal-shape curve that retraces on the return sweep (Fig. 4.10).

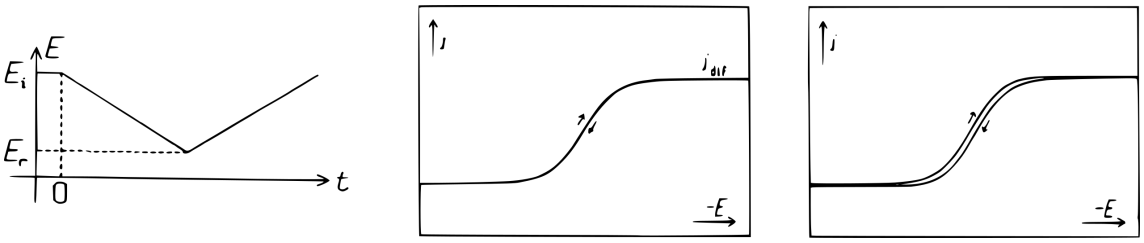

Figure 4.10: From left to right: potential waveform with a sweep between the initial potential (E_i) and the reversal potential (E_r); steady-state current vs. potential curves showing the symmetrical sigmoidal shape.

Thorough voltammetric studies of potassium ferrocyanide [$K_4Fe(CN)_6$] and ferricyanide [$K_3Fe(CN)_6$] in aqueous solution were fully investigated in the past [70, 82, 55], in order to detect the chemically reversible $[Fe(CN)_6]^{3-/4-}$ couple.

Following the steps made by van Rossem et al. [51], in this study the oxygen sensor was characterized electrochemically by CV cycles in presence of the potassium ferricyanide redox couple in concentrations of 2, 4 and 8 mM in a 0.1 M of PBS. Therefore, at the WE surface the reduction reaction of the $[Fe(CN)_6]^{3-}$ ion took place [55]:

$$[Fe(CN)_6]^{3-} + e^- \longrightarrow [Fe(CN)_6]^{4-} \tag{4.1}$$

In this study, due to the limited time frame and very high superimposed noise, the performance of the only variant with 256 UMEs and 4 μm diameter was investigated since it gave the highest signal. All the measurements were performed using VersaSTAT 4 potentiostat (Ametek Scientific Instruments) with external platinum counter electrode (CE) and saturated Ag/AgCl reference electrode (RE).

Hence, the voltage was swept in the range [0V; 0.5 V] vs. the Ag/AgCl reference electrode with a scan-rate of 100 mV/s. After smoothing the curves by removing a quite high superimposed noise probably due to the magnetic stirrer used, the derived CVs are shown in Fig. 4.11. The variations of the steady state current intensity as a function of the ferricyanide concentration were studied and compared with the expected response.

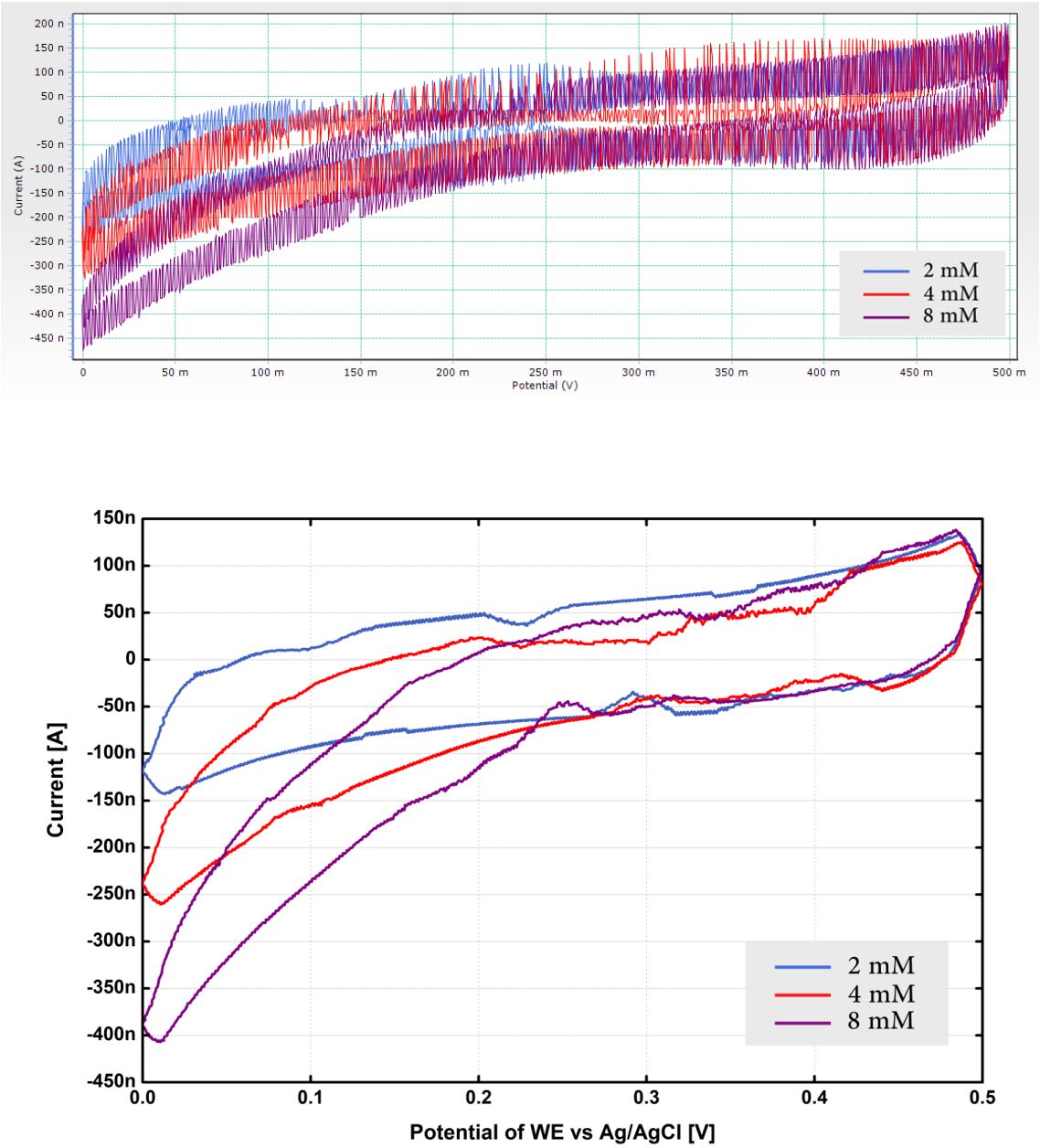

Figure 4.11: CV waves for the different ferricyanide concentrations by sweeping the voltage in the range [0V; 0.5 V] vs. the Ag/AgCl reference electrode with a scan-rate of 100 mV/s. On top the original curves obtained from measurements, on the bottom the smoothed ones.

Recalling Eq. 1.24, considering the number of electrons involved in the reaction equal to 1 (as noticeable from Eq. 4.1) and assuming a recess depth of 3 μm and a diffusion coefficient for ferricyanide of $8.12 \cdot 10^{-6}$ cm^2/s (for a 0.1 M KCl solution at 20° C) as suggested by Keeley et al. [83], a comparison between experimental and theoretical values was done as shown in Tab. 4.3:

$K_4Fe(CN)_6$ [mM]	diameter [μm]	UMEs [number]	$i_{ss,theo}$ [nA]	$i_{ss,meas}$ [nA]	Error [%]
2	4	256	-110.3	-170	54.1%
4	4	256	-220.6	-250	13.3%
8	4	256	-441.1	-400	9.3%

Table 4.3: Comparison between the experimental and the theoretical steady-state currents for the reduction of potassium ferricyanide for solutions with varying concentrations 2, 4 and 8 mM.

As can be seen from the CVs, the curves did not look like to the expected sigmoids as described in literature [55, 70]: a consistent gap between the forward and backward branches was present, indicating that either the sweep rate was too fast or that a poor seal was present between the insulator and the platinum electrode.

This can be attributed also to a superimposed noise, which compromised the original data, including the determination of the $i_{ss,meas}$. Indeed, although the current response values in Tab. 4.3 were very rough approximations, they scaled with the ferricyanide concentration, as described by the theory (Fig. 4.12).

Moving forward to the measurement setup, the polarization voltage for the oxygen reduction was determined using CV measurements under atmospheric conditions (21% oxygen or 7.8 mg/mL [48]) in a PBS solution within the voltage range of [-1 V; 1 V] vs. the Ag/AgCl reference electrode and with a scan-rate of 100 mV/s.

The CV curve was in line with previous works [51, 84], as the values of the oxidized/reduced current peaks occurred approximately at the same applied potential, with a slight shift towards negative voltages (Fig. 4.13). The resulting graph showed that the potential range where the oxygen reduction took place was between -0.8 and -0.2 V vs. Ag/AgCl. Within this window, -0.5 V was chosen as the polarization

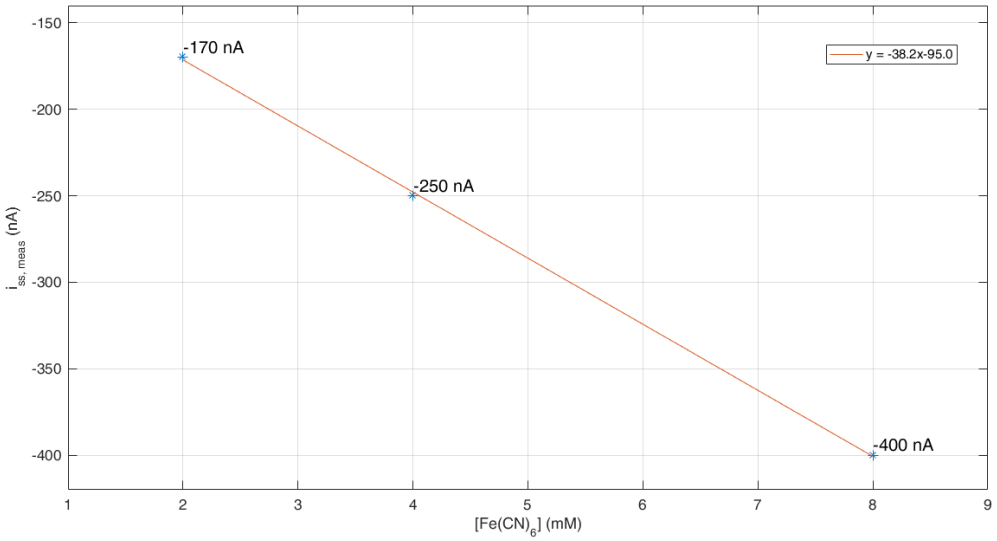

Figure 4.12: Variations of the steady-state current as a function of the ferricyanide concentration (scattered points), with the corresponding regression curve (solid line).

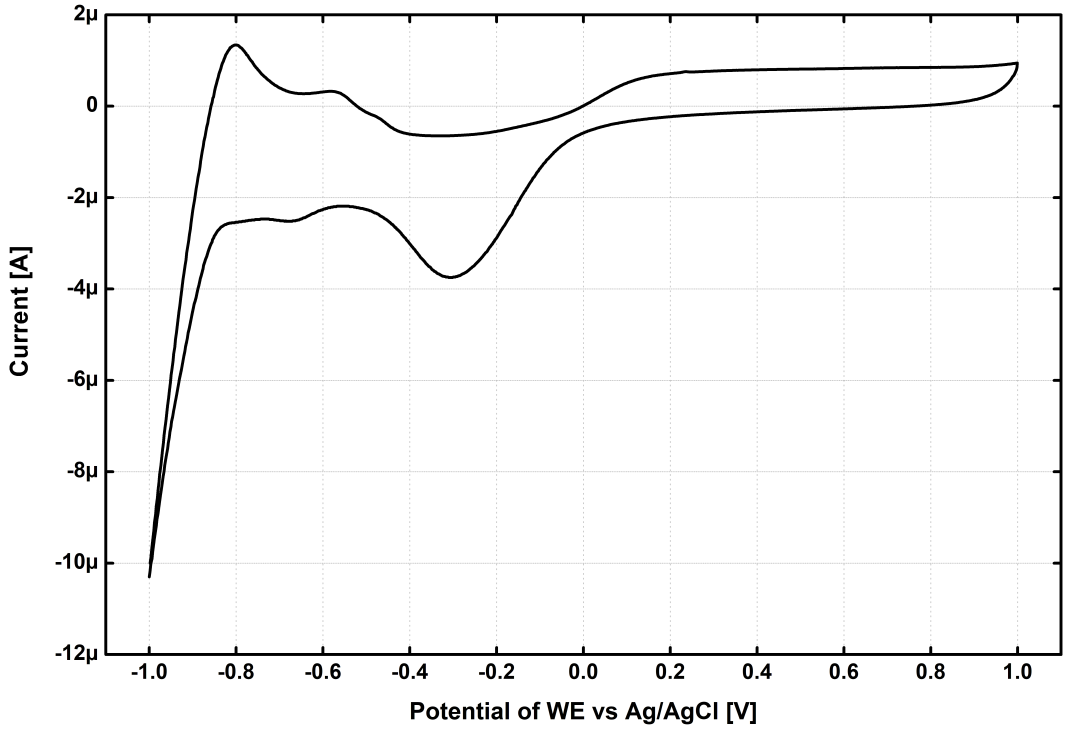

Figure 4.13: Determination of the polarization potential for the reduction of oxygen using CVs recorded in PBS under atmospheric conditions a scan-rate of 100 mV/s.

voltage for further characterization measurements.

Unfortunately, additional measurements could not be feasible, due to lack of appropriate equipment suitable for injecting precise amounts of oxygen. Indeed, instruments like mass flow controllers are indispensable in these kind of experiments, as well as oxygen and nitrogen dispensers and a commercial Clark-type oxygen sensor. Nevertheless, the designed UMEA seemed to be a very promising oxygen sensor, as good results in characterization protocols were achieved.

4.5 Temperature Sensor

The electrical resistance was measured by varying temperatures from 15° to 70° C and collecting data every 5° C, adopting the aforementioned 2-wire configuration (Section 1.6.1) and using a LCR meter (4284A Agilent). In order to test the accuracy of the instrument, a 82 Ω resistor was used and the value of 82.76 Ω was read by using the LCR meter. During both calibration and measurements, the ambient temperature of the room was constant and fixed to 21.7° C.

For the calibration setup, the variants were dipped in a beaker filled with PBS which was heated upon a hotplate. The actual temperature of the solution was monitored with a commercial type K thermocouple (AZ8852 K/J/T Thermometer). The value of resistance was measured for each designed variant, specifically Pt 100, Pt 500 and Pt 1000 with polyimide as protection coating. Moreover, the Pt 100 with parylene-C layer was considered, in order to compare the results of the two different materials used. The graphs and the linear relationship between resistance and temperature (Eq. 1.16) are shown in Fig. 4.14.

Characterization of the RTDs showed the resistance of the sensor to increase linearly with temperature in the studied range of 15°-70° C. For each variant, the nominal resistance $R_{20°C}$ was derived and compared to the theoretical value. Hence, the sensitivities and the PTCs α values were calculated as exhibited in Tab. 4.4.

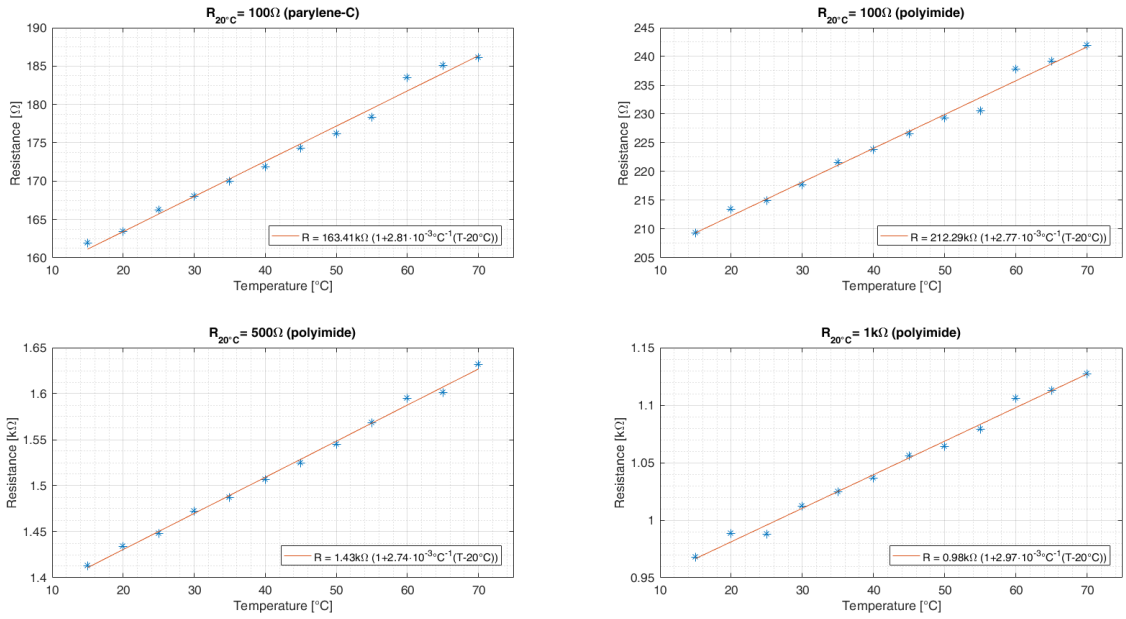

Figure 4.14: Electrical resistance vs. temperature for RTDs dipped in PBS with $R_{20°C}$ values of 100 Ω, 500 Ω and 1000 Ω (scattered points), each with their own theoretical regression curve (solid lines).

Coating	$R_{20°C\,theo}$ [Ω]	$R_{20°C\,meas}$ [Ω]	Sensitivity [Ω/°C]	α [1/°C]
parylene-C	100	163.4	0.46	$2.81{\cdot}10^{-3}$
polyimide	100	213.4	0.59	$2.77{\cdot}10^{-3}$
polyimide	500	1434.0	3.93	$2.74{\cdot}10^{-3}$
polyimide	1000	988.6	2.92	$2.97{\cdot}10^{-3}$

Table 4.4: Comparison of for each sample features found out during the characterization setup.

In order to examine the deviation of the measured data from the theoretical ones, the root-mean-square errors (RMSEs) were calculated and gave quite similar results to previous studies: 0.839 Ω/°C, 0.997 Ω/°C, 3.883 Ω/°C, 4.431 Ω/°C (listed in the same order as in the Tab. 4.4).

The nominal resistances at 20° C were higher than expected, except the Pt 1000 sample which was slightly lower and might have to do with the non-idealities encountered during the fabrication process. The measured value of the Pt 500 stood out, since it was found to be almost the triple of the theoretical one. The most likely

hypothesis was the presence of a parasitic contribution caused by the wire bonding.

The found sensitivity values, which corresponded to the slopes ($slope = \alpha \cdot R_{20°C}$), were almost the double of the theoretical ones concerning the Pt 100s, meanwhile for Pt 500 and Pt 1000 they were almost the same. In fact, if $R_{20°C\,meas}$ values were normalized with respect to the theoretical ones, hence, the expected sensitivities were calculated as the product of the derived PTCs and the $R_{20°C\,theo}$, the following values were obtained: 0.281 Ω/°C, 0.277 Ω/°C, 3.7 Ω/°C, 2.97 Ω/°C (listed in the same order as in the Tab. 4.4). The sample that showed the highest sensitivity was the Pt 500, since it is directly proportional to the nominal resistance $R_{20°C}$.

The PTC values were comparable among the variants, even if they were lower than the theoretical $3.9 \cdot 10^{-3}$/°C of pure platinum. However, application of an adhesion layer between the wafer substrate and the platinum strip is known to further reduce this coefficient [7]. The obtained values were proven to be comparable to reported studies [85].

Considering the two Pt 100s with different isolation layers, the behavior was quite the same, showing a difference of 50 Ω in the nominal resistance and a deviation of 1.4% in the PTC value. In such analysis, it would be careless to draw conclusions, since only two samples were tested. In a more deepened study, several samples should be taken into consideration. Moreover, the same applies to the calibration setup: the values of resistance should be measured several times in order to determine their repeatability.

Once completed the sensor characterization, the PTC and $R_{20°C}$ values were taken as reference for the subsequent measurements. In this regard, the response of each sample was studied by applying some drops of yeast culture with concentration of 10 g/l and 70 g/l and by looking at the resistance value after 60 seconds (Fig. 4.15). Even in this case, it was hard to draw conclusions due to few samples tested. However, it was worthwhile noticing that the resistance values changed slowly after the application of the yeast solutions and did not stabilized. Supposing that the temperature of the solution was stable and at the same temperature of the room, this would indicate that the time response of the sensors was higher than 60

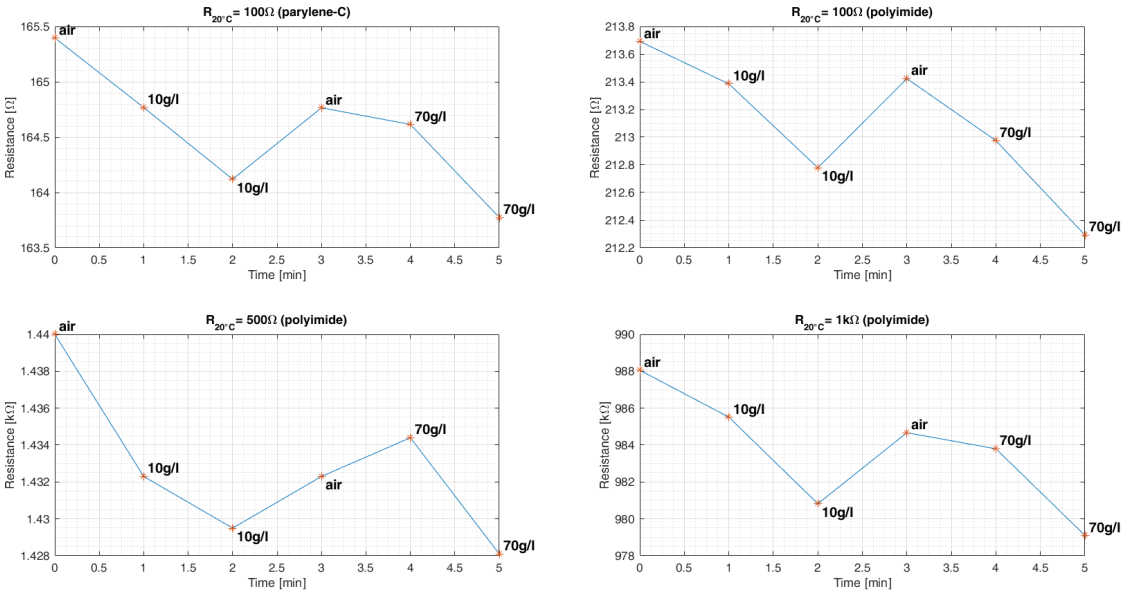

Figure 4.15: Resistance vs. time monitoring in a measurement setup of yeast solution with concentration of 10 g/L and 70 g/L.

seconds. Unfortunately, because of lack of time, there was not the opportunity to repeat the measurements by tracking the resistance in a wider time window. In further analysis this modification of the measurement setup should be taken into consideration; namely anytime a new solution is applied, the resistance should be monitored until its value stabilizes. This final value, then, should be taken as reference for the specific solution, in order to recalibrate the RTD.

Chapter 5

Conclusions

In this thesis, an integrated multi-sensor biochip for in-situ monitoring of glucose, lactate, cell density, pH, oxygen and temperature in biotechnological processes was developed. In this work, the integration of such a high number of sensors and simultaneously the adoption of a low cost and straightforward production line had not been demonstrated before to the author's best knowledge.

All sensor elements were characterized and most of them showed good results comparable to those described in literature. They all sound promising, except the glucose sensor, whose functionalization procedure needs to be reexamined. Further improvements in the fabrication steps may be done thereby solving the bad adhesion problem for silver after the polyimide etching and, besides, using a different material for bond pads (e.g., aluminum instead of gold) to have a better long-term wire bonding, as well as a lower-cost solution.

The choice of integrating several sensor elements in a single chip lies on the need of detecting different parameters. Moreover, the close proximity of all the sensors allows to obtain more reliable data, since information extracted from different sensors may be complemented each other. In this case study, for example, pH and temperature are known to significantly influence most of the biological processes. Therefore, the data extrapolated from the respective sensors could be used to compensate all the others.

Furthermore, the small chip area is also a requirement for integration reasons. In fact, the advent of single-use technologies has led to monitor small volume products.

Another essential requirement for a biochip is the sterility. Indeed, in order not to either contaminate or kill the cells, every item introduced into a bioreactor has to be sterilized (e.g., gamma ray, e-beam irradiation). Unfortunately this was not possible to inspect in this work given the limited time frame of this master's dissertation. Nevertheless, investigation into long-term stability of sterilized sensors is necessary to reach commercial maturity.

In this regard, a complete measurement system could be achieved by integrating a readout circuit, instead of using a simple header interface to cumbersome external control equipment. A customized integrated circuit would allow users to handily acquire real-time data, by simply interacting with a user-friendly software. Moreover, parassitisms introduced by long probes connecting the chip to the external instrumentation would be definitely reduced. An other advantage with respect to using external equipment is the non-limited information about their circuitry and behavior. Indeed, home-made readout circuits can be modified as needed for varying applications, hence not operating as *black boxes*.

Although the sensor elements developed in this work require different measurement setup, thus different expensive and cumbersome instruments, a low-cost and handy solution could be implemented. The idea is to design a device that would be able to match all of the measurement setup and all of the specifications required by each used equipment.

A simple overview of a likely integrated readout circuit implementation is shown in Fig. 5.1. The circuit is designed to control and power a microcontroller with a USB connection, allowing interaction with a computer. The operating principle lays on a well-known potentiostatic circuit, since, due to its application, it is a general-purpose tool. It is interfaced to a recognizable three-electrode electrochemical cell, which includes a working electrode (WE), a counter electrode (CE) and a reference electrode (RE). In this setup, amperometric measurements would be performed as seen in the case of the glucose and oxygen sensors. Concerning the potentiometric

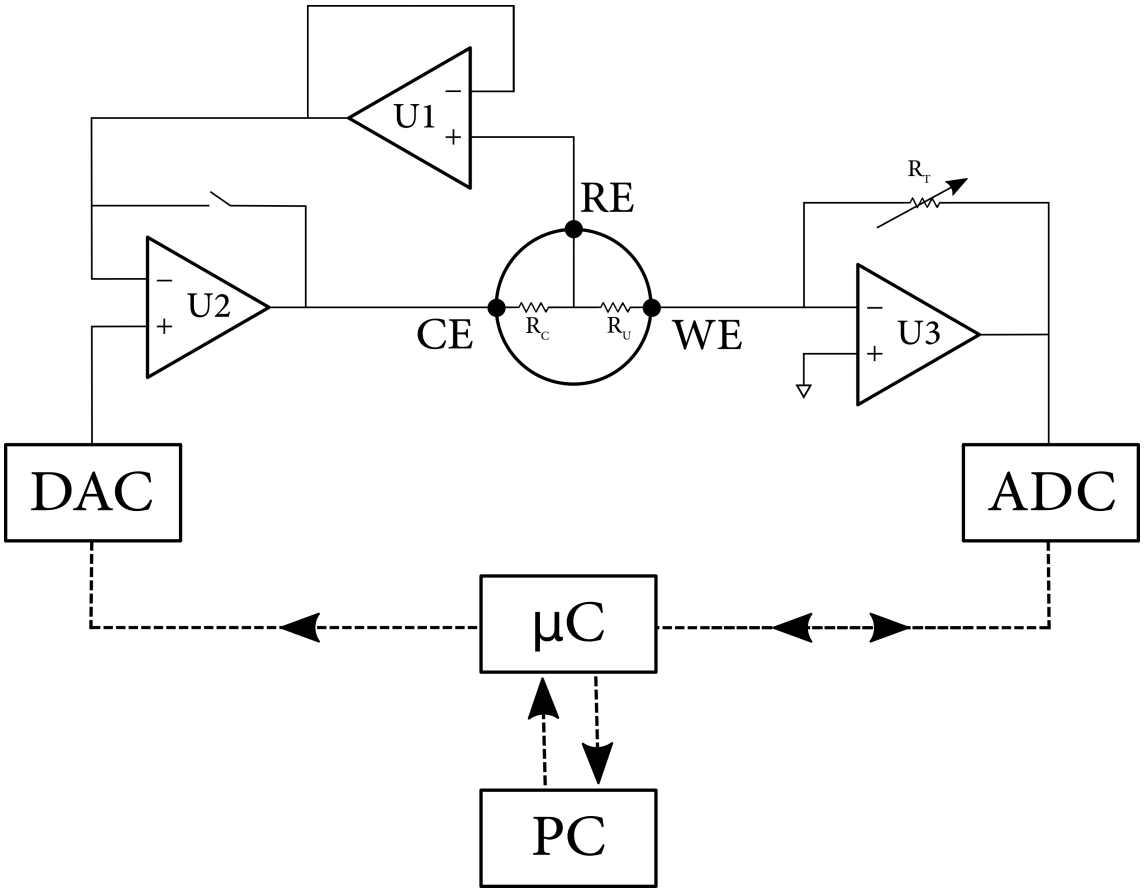

Figure 5.1: Schematic overview of a likely readout circuit, including the digital-to-analog converter (DAC), the analog-to-digital converter (ADC), the microcontroller (μC), the computer (PC) and interfacing to a three-electrode electrochemical cell, which includes a working electrode (WE), a counter electrode (CE) and a reference electrode (RE). Analog connections are represented by solid lines, digital ones by dotted arrows.

analysis used for the pH sensor, it is necessary to simply short circuit the RE and the CE with a switch. Finally for the RTD and cell density electrodes, the same setup of the pH sensor could be used, but a reprogram of the microcontroller is required.

The three-electrode electrochemical cell is modeled as two resistances in series, between CE and RE (R_c, compensated cell resistance) and between RE and WE (R_u, uncompensated cell resistance). The RE and CE are in a negative feedback loop regulated by op-amp U2 which is able to supply the current required to compensate the so-called *IR drop* across R_c (as previously described in Section 1.2.1). Moreover,

an additional op-amp U1 was inserted as unity gain buffer to limit any current that might flow through RE. Both the op-amps should be selected considering large open loop gains, small voltage noise densities and offsets and small input bias currents, in order to have voltage signals as accurate as possible.

The potential between WE and RE can be set by biasing the circuit with a digital to analog converter (DAC), controlled by the microcontroller. In this case, the choice relies on small quantization error, hence on high resolution, as well as on high sample rate and good reconstruction filter.

To avoid aliasing problems and to have high signal resolution, the same specifications should be considered for the analog to digital converter (ADC), which is fundamental for recording digital data through a computer.

A transimpedance amplifier (U3) is indispensable between the WE and the ADC, since the current passing through the WE has to be converted to a voltage that will be read by the ADC. Additionally, because ADCs are not able to detect an infinitely large range of voltages, different values of the transimpedance resistor R_M are necessary. Therefore, instead of using a single resistor that would limit the magnitude of currents of interest, the addition of a multiplexer handling different resistor would be a smart solution. In this stage, the main requirement for the transimpedance op-amp is a very small input bias current, since it is superimposed to the signal current.

Finally, the microcontroller unit should be chosen to guarantee the proper operation of the digital components: updating the DAC at the necessary rate, acquiring the ADC collected data, selecting the resistors of the multiplexer and managing all the switches.

Preliminary specifications for a readout circuit for the developed sensor elements are listed in Tab. 5.1, basing on both theoretical calculations and references from literature, used equipment settings and obtained measurement results.

Sensor	Specification	Value
Enzyme	Measurement principle	Amperometric
	Voltage between WE and RE	700 mV
	Current measurement range	0 - 500 nA
	Current resolution	1 nA
Cell density	Measurement principle	Impedance spectroscopy
	Frequency range	1 kHz - 30 MHz
	Impedance range	100 Ω - 300 Ω
	Impedance resolution	$\leq$ 0.5 %
pH	Measurement principle	Potentiometric
	Voltage measurement range	-30 mV - 600 mV
	Voltage resolution	1 mV
Oxygen	Measurement principle	Amperometric
	Voltage between WE and RE	-500 mV
	Current measurement range	-500 nA - 200 nA
	Current resolution	1 nA
	Sampling time	24 μs
Temperature	Measurement principle	Impedance analysis
	Resistance measurement range	100 Ω - 2 kΩ
	Resistance resolution	10 mΩ
	Maximum current	100 mA

Table 5.1: Preliminary specifications for a readout circuit for the developed sensor elements.

List of Figures

List of Tables

Bibliography

[1] M. Flickinger, *Upstream Industrial Biotechnology.* Wiley, 2013.

[2] C. H. Ahn, J. W. Choi, G. Beaucage, J. H. Nevin, J. B. Lee, A. Puntambekar, and J. Y. Lee, "Disposable smart lab on a chip for point-of-care clinical diagnostics," *Proceedings of the IEEE*, vol. 92, no. 1, pp. 154–173, 2004.

[3] S. Mross, T. Zimmermann, N. Winkin, M. Kraft, and H. Vogt, "Integrated multi-sensor system for parallel in-situ monitoring of cell nutrients, metabolites and cell mass in biotechnological processes," *Procedia Engineering*, vol. 120, pp. 372–375, 2015. [Online]. Available: http://dx.doi.org/10.1016/j.snb.2016.03.086

[4] R. Eibl, *Single-Use Biopharmaceutical Technology In Manufacture.* Wiley, 2011.

[5] A. A. Shukla and U. Gottschalk, "Single-use disposable technologies for biopharmaceutical manufacturing," *Trends in Biotechnology*, vol. 31, no. 3, pp. 147–154, 2013. [Online]. Available: http://dx.doi.org/10.1016/j.tibtech.2012.10.004

[6] É. D. Vieira, M. Da Graça Stupiello Andrietta, and S. R. Andrietta, "Yeast biomass production: A new approach in glucose-limited feeding strategy," *Brazilian Journal of Microbiology*, vol. 44, no. 2, pp. 551–558, 2013.

[7] E. E. Krommenhoek, J. G. Gardeniers, J. G. Bomer, X. Li, M. Ottens, G. W. Van Dedem, M. Van Leeuwen, W. M. Van Gulik, L. A. Van Der Wielen, J. J. Heijnen, and A. Van Den Berg, "Integrated electrochemical sensor array for on-line monitoring of yeast fermentations," *Analytical Chemistry*, vol. 79, no. 15, pp. 5567–5573, 2007.

[8] E. E. Krommenhoek, M. van Leeuwen, H. Gardeniers, W. M. van Gulik,

A. van den Berg, X. Li, M. Ottens, L. A. van der Wielen, and J. J. Heijnen, "Lab-Scale Fermentation Tests of Microchip With Integrated Electrochemical Sensors for pH, Temperature, Dissolved Oxygen and Viable Biomass Concentration," *Wiley InterScience*, vol. 99, no. 4, pp. 884–892, 2008.

[9] S. Mross, P. Fürst, S. Pierrat, T. Zimmermann, H. Vogt, and M. Kraft, "Enzyme Sensor With Polydimethylsiloxane Membrane and CMOS Potentiostat for Wide-Range Glucose Measurements," *IEEE Sensors Journal*, vol. 15, no. 12, pp. 7096–7104, 2015.

[10] Y. Qin, A. U. Alam, S. Pan, M. M. Howlader, R. Ghosh, N. X. Hu, H. Jin, S. Dong, C. H. Chen, and M. J. Deen, "Integrated water quality monitoring system with pH, free chlorine, and temperature sensors," *Sensors and Actuators, B: Chemical*, vol. 255, pp. 781–790, 2018.

[11] P. Salvo, N. Calisi, B. Melai, B. Cortigiani, M. Mannini, A. Caneschi, G. Lorenzetti, C. Paoletti, T. Lomonaco, A. Paolicchi, I. Scataglini, V. Dini, M. Romanelli, R. Fuoco, and F. Di Francesco, "Temperature and pH sensors based on graphenic materials," *Biosensors and Bioelectronics*, vol. 91, no. January, pp. 870–877, 2017. [Online]. Available: http://dx.doi.org/10.1016/j.bios.2017.01.062

[12] F. Gódia and J. Cairó, "Cell Metabolism," *Cell Culture Technology for Pharmaceutical and Cell-Based Therapies*, pp. 81–112, 2005.

[13] T. L. N. M. Pohlscheidt, S. Charaniya, C. Bork, M. Jenzsch, Luebbert, and A., "Bioprocess and Fermentation Monitoring," *Upstream Industrial Biotechnology*, pp. 1471–1491, 2013.

[14] R. H. Baltz, J. E. Davies, and A. L. Demian, *Manual of Industrial Biotechonolgy*. ASM, 2010.

[15] J. N. Lisbeth Olsson, Ulrik Schulze, "On-line bioprocess monitoring ˆ an academic discipline or an industrial tool?" *analytical chemistry*, vol. 17, pp. 88–94, 1998.

[16] M. D.A., K. N., and B. M., *Solid-state fermentation bioreactors*. Springer, 2006.

[17] S. Hauttmann and J. Müller, "In-situ biomass characterisation by impedance

spectroscopy using a full-bridge circuit," *Bioprocess and Biosystems Engineering*, vol. 24, no. 3, pp. 137–141, 2001.

[18] S. S. Ozturk and W.-s. Hu, *Cell Culture Technology for Pharmaceutical and Cell-Based Therapies*. CRC Press, 2006.

[19] D. Prescott, *Methods in cell biology*. Academic Press, 1975.

[20] J. Luo, T. Dziubla, and R. Eitel, "A low temperature co-fired ceramic based microfluidic Clark-type oxygen sensor for real-time oxygen sensing," *Sensors and Actuators, B: Chemical*, vol. 240, pp. 392–397, 2017.

[21] M. U. Ahmed, M. M. Hossain, and E. Tamiya, "Electrochemical biosensors for medical and food applications," *Electroanalysis*, vol. 20, no. 6, pp. 616–626, 2008.

[22] S. Mross, "Integrated Multi-Sensor System for Parallel In-Situ Monitoring of Biotechnological Processes," *Sensors and Actuators B*, 2016.

[23] S. Mross, T. Zimmermann, S. Zenzes, M. Kraft, and H. Vogt, "Study of enzyme sensors with wide, adjustable measurement ranges for in-situ monitoring of biotechnological processes," *Sensors and Actuators, B: Chemical*, vol. 241, pp. 48–54, 2017. [Online]. Available: http://dx.doi.org/10.1016/j.snb.2016.10.054

[24] M. Baghayeria, H. Veisi, and M. Ghanei-Motlagh, "Amperometric glucose biosensor based on immobilization of glucose oxidase on a magnetic glassy carbon electrode modified with a novel magnetic nanocomposite," *Sensors and Actuators B: Chemical*, vol. 249, pp. 321–330, 2017. [Online]. Available: http://dx.doi.org/10.1016/j.snb.2017.04.100

[25] N. J. Ronkainen, H. B. Halsall, and W. R. Heineman, "Electrochemical biosensors," *Chemical Society Reviews*, vol. 39, no. 5, pp. 1747–1763, 2010.

[26] A. Liebman, Joel; Greenberg, "Structure Energetics and Reactivity in Chemistry Series," *Free Radical Biology and Medicine*, 1995.

[27] J. Janata, *Principles of Chemical Sensors*. Springer, 2009.

[28] A. J. Bard and L. R. Faulkner, *Electrochemical Methods: Fundamentals And Applications*. Wiley, 2001.

[29] C. G. Zoski, *Handbook of Electrochemistry*. Elsevier, 2007.

[30] M. Alvarez-Icaza and U. Bilitewski, "Mass Production of Biosensors," *Analytical*

Chemistry, vol. 65, no. 11, pp. 525–533, 1993.

[31] M. Koudelka, S. Gernet, and N. F. De Rooij, "Planar amperometric enzyme-based glucose microelectrode," *Sensors and Actuators*, vol. 18, no. 2, pp. 157–165, 1989.

[32] Y. Xu, A. S. Jeevarajan, J. M. Fay, T. D. Taylor, and M. M. Anderson, "On-Line Measurement of Glucose in a Rotating Wall Perfused Vessel Bioreactor Using an Amperometric Glucose Sensor [Journal of The Electrochemical Society, 149, H103 (2002)]," *Journal of The Electrochemical Society*, vol. 149, no. 8, p. L5, 2002.

[33] R. Vaidya and E. Wilkins, "Effect of interference on amperometric glucose biosensors with cellulose acetate membranes," *Electroanalysis*, vol. 6, no. 8, pp. 677–682, 1994.

[34] A. Maines, D. Ashworth, and P. Vadgama, "Diffusion restricting outer membranes for greatly extended linearity measurements with glucose oxidase enzyme electrodes," *Analytica Chimica Acta*, vol. 333, no. 3, pp. 223–231, 1996.

[35] D. J. Harrison, R. F. Turner, and H. P. Baltes, "Characterization of Perfluorosulfonic Acid Polymer Coated Enzyme Electrodes and a Miniaturized Integrated Potentiostat for Glucose Analysis in Whole Blood," *Analytical Chemistry*, vol. 60, no. 19, pp. 2002–2007, 1988.

[36] A. P. Soldatkin, A. V. El'skaya, A. A. Shul'ga, A. S. Jdanova, S. V. Dzyadevich, N. Jaffrezic-Renault, C. Martelet, and P. Clechet, "Glucose sensitive conductometric biosensor with additional Nafion membrane: reduction of influence of buffer capacity on the sensor response and extension of its dynamic range," *Analytica Chimica Acta*, vol. 288, no. 3, pp. 197–203, 1994.

[37] K. Asami and T. Yonezawa, "Dielectric analysis of yeast cell growth," *BBA - General Subjects*, vol. 1245, no. 1, pp. 99–105, 1995.

[38] K. Asami, "Characterization of heterogeneous systems by dielectric spectroscopy," *Progress in Polymer Science (Oxford)*, vol. 27, no. 8, pp. 1617–1659, 2002. [Online]. Available: http://www.sciencedirect.com/science/article/pii/S0022309302011109

[39] M. Ibrahim, J. Claudel, D. Kourtiche, and M. Nadi, "Geometric

parameters optimization of planar interdigitated electrodes for bioimpedance spectroscopy," *Journal of Electrical Bioimpedance*, vol. 4, no. 1, pp. 13–22, 2013. [Online]. Available: https://www.journals.uio.no/index.php/bioimpedance/article/view/304

[40] R. E. van Hal, J. C. Eijkel, and P. Bergveld, "A novel description of ISFET sensitivity with the buffer capacity and double-layer capacitance as key parameters," *Sensors and Actuators: B. Chemical*, vol. 24, no. 1-3, pp. 201–205, 1995.

[41] F. Li, N. Vijayasankaran, A. Shen, R. Kiss, and A. Amanullah, "Cell culture processes for monoclonal antibody production," 2010.

[42] A. U. Alam, Y. Qin, S. Nambiar, J. T. Yeow, M. M. Howlader, N. X. Hu, and M. J. Deen, "Polymers and organic materials-based pH sensors for healthcare applications," *Progress in Materials Science*, vol. 96, no. August 2017, pp. 174–216, 2018.

[43] Y. Qin, H. J. Kwon, M. M. Howlader, and M. J. Deen, "Microfabricated electrochemical pH and free chlorine sensors for water quality monitoring: Recent advances and research challenges," *RSC Advances*, vol. 5, no. 85, pp. 69 086–69 109, 2015. [Online]. Available: http://dx.doi.org/10.1039/C5RA11291E

[44] B. Lakard, G. Herlem, S. Lakard, R. Guyetant, and B. Fahys, "Potentiometric pH sensors based on electrodeposited polymers," *Polymer*, vol. 46, no. 26, pp. 12 233–12 239, 2005.

[45] Roger G Bates, *Determination of pH: theory and practice*, 1973.

[46] O. Korostynska, K. Arshak, E. Gill, and A. Arshak, "State Key Laboratory of Nonlinear Mechanics (LNM), Institute of Mechanics, Chinese Academy of Sciences, Beijing 100080, China," *Sensors*, vol. 7, no. 12, pp. 3027–3042, 2007. [Online]. Available: http://www.mdpi.com/1424-8220/7/12/3027

[47] "www.eidusa.com/Theory_DO.htm."

[48] Alliance Technical Sales, "A Guide to Oxygen Measurement: Theory and Practice of Oxygen Applications," 2016.

[49] Leland C. Clark, "Electrochemical Device For Chemical Analysis," 1956.

[50] Leland C. Clark, R. Wolf, D. Granger, and Z. Taylor, "Continuos Recording of Blood Oxygen Tensions by Polarography," *Journal of Applied Physiology*, vol. 6, no. 3, pp. 189–193, 1953.

[51] F. van Rossem, J. G. Bomer, H. L. D. Boer, Y. Abbas, E. D. Weerd, A. V. D. Berg, and S. Le, "Sensing oxygen at the millisecond time-scale using an ultramicroelectrode array (UMEA)," vol. 238, pp. 1008–1016, 2017.

[52] A. M. Bond, D. Luscombe, K. B. Oldham, and C. G. Zoski, "A comparison of the chronoamperometric response at inlaid and recessed disc microelectrodes," *Journal of Electroanalytical Chemistry*, vol. 249, pp. 1–14, 1988.

[53] K. B. Oldham and C. G. Zoski, "Steady-state voltammetry at an inlaid microdisc: comparison of three approaches," *Journal of Electroanalytical Chemistry*, vol. 313, no. 1-2, pp. 17–28, 1991.

[54] C. G. Zoski, "A survey of steady-state microelectrodes and experimental approaches to a voltammetric steady state," *Journal of Electroanalytical Chemistry*, vol. 296, no. 2, pp. 317–333, 1990.

[55] ——, "Ultramicroelectrodes : Design , Fabrication , and Characterization," pp. 1041–1051, 2002.

[56] C. G. Zoski, A. M. Bond, C. L. Colyer, J. C. Myland, and K. B. Oldham, "Near-steady-state cyclic voltammetry at microelectrodes," *Journal of Electroanalytical Chemistry*, vol. 263, no. 1, pp. 1–21, 1989.

[57] P. Regtien and E. Dertien, *Resistive sensors*, 2018. [Online]. Available: https://linkinghub.elsevier.com/retrieve/pii/B9780128138106000045

[58] W. Y. Du, *Resistive, Capacitive, Inductive, and Magnetic Sensor Technologies*, 2015.

[59] National Instruments Corporation, "Measuring Temperature with RTDs – A Tutorial," *Configurations*, no. November, 1996.

[60] S. Mross, S. Pierrat, T. Zimmermann, and M. Kraft, "Microfluidic enzymatic biosensing systems: A review," *Biosensors and Bioelectronics*, vol. 70, pp. 376–391, 2015.

[61] W. Olthuis, W. Streekstra, and P. Bergveld, "Theoretical and experimental determination of cell constants of planar-interdigitated electrolyte conductivity

sensors," *Sensors and Actuators: B. Chemical*, vol. 24, no. 1-3, pp. 252–256, 1995.

[62] G. Langereis, *An integrated sensor system for monitoring washing processes*, 1999.

[63] L. Florea, C. Fay, E. Lahiff, T. Phelan, N. E. O'Connor, B. Corcoran, D. Diamond, and F. Benito-Lopez, "Dynamic pH mapping in microfluidic devices by integrating adaptive coatings based on polyaniline with colorimetric imaging techniques," *Lab on a Chip*, vol. 13, no. 6, pp. 1079–1085, 2013.

[64] T. Lindfors and A. Ivaska, "pH sensitivity of polyaniline and its substituted derivatives," *Journal of Electroanalytical Chemistry*, vol. 531, no. 1, pp. 43–52, 2002.

[65] H. Bai and G. Shi, "Gas Sensors Based on Conducting Polymers," *Sensors*, pp. 267–307, 2007.

[66] H. S. Abdulla and A. I. Abbo, "Optical and electrical properties of thin films of polyaniline and polypyrrole," *International Journal of Electrochemical Science*, vol. 7, no. 11, pp. 10 666–10 678, 2012.

[67] N. Vanonckelen, "Interfacing digital microfluidics with potentiometric detection techniques," Ph.D. dissertation, 2016.

[68] Y. Wei, R. Hariharan, and S. A. Patel, "Chemical and electrochemical copolymerization of aniline with alkyl ring-substituted anilines," *Macromolecules*, vol. 23, no. 3, pp. 758–764, 1990.

[69] C. Belmont, M. L. Tercier, J. Buffle, G. C. Fiaccabrino, and M. Koudelka-Hep, "Mercury-plated iridium-based microelectrode arrays for trace metals detection by voltammetry: Optimum conditions and reliability," *Analytica Chimica Acta*, vol. 329, no. 3, pp. 203–214, 1996.

[70] J. Orozco, C. Fernández-Sánchez, and C. Jiménez-Jorquera, "Ultramicroelectrode array based sensors: A promising analytical tool for environmental monitoring," *Sensors*, vol. 10, no. 1, pp. 475–490, 2010.

[71] J. Maruyama, M. Inaba, and Z. Ogumi, "Rotating ring-disk electrode study on the cathodic oxygen reduction at Nafion®-coated gold electrodes," *Journal of Electroanalytical Chemistry*, vol. 458, no. 1-2, pp. 175–182, 1998.

[72] N. F. Al Zubaidi Mohammad, Josep Sule Suso, "Precision control of dissolved oxygen in mammalian cell culture media impacts on in situ volatile genera- tion and promotes improved mesenchymal stem cell yield accompanied by reduced transcriptional variability Al," *Free Radical Biology and Medicine*, vol. 86, p. 2015, 2015.

[73] V. Karagounis, L. Lun, and C. Liu, "A thick-film multiple component cathode three-electrode oxygen sensor," *IEEE Transactions on Biomedical Engineering*, vol. BME-33, no. 2, pp. 108–112, Feb 1986.

[74] R. Murji and M. J. Deen, "A scalable meander-line resistor model for silicon RFICs," *IEEE Transactions on Electron Devices*, vol. 49, no. 1, pp. 187–190, 2002.

[75] R. A. Serway, *Principles of Physics*, 1998.

[76] N. Elgrishi, K. J. Rountree, B. D. McCarthy, E. S. Rountree, T. T. Eisenhart, and J. L. Dempsey, "A practical beginner's guide to cyclic voltammetry," *Journal of Chemical Education*, vol. 95, no. 2, pp. 197–206, 2018. [Online]. Available: https://doi.org/10.1021/acs.jchemed.7b00361

[77] M. Bäcker, S. Beging, M. Biselli, A. Poghossian, J. Wang, W. Zang, P. Wagner, and M. J. Schöning, "Concept for a solid-state multi-parameter sensor system for cell-culture monitoring," *Electrochimica Acta*, vol. 54, no. 25, pp. 6107–6112, 2009.

[78] B. Timmer, W. Sparreboom, W. Olthuis, P. Bergveld, and A. Van den Berg, "Optimization of an electrolyte conductivity detector for measuring low ion concentrations," *Lab on a Chip*, vol. 2, no. 2, pp. 121–124, 2002.

[79] M. Bäcker, S. Pouyeshman, T. H. Schnitzler, A. Poghossian, P. Wagner, M. Biselli, and M. J. Schöning, "A silicon-based multi-sensor chip for monitoring of fermentation processes," *Physica Status Solidi (A) Applications and Materials Science*, vol. 208, no. 6, pp. 1364–1369, 2011.

[80] S. Prajapati, "Everything You Need to Know About pH Sensor Calibration." [Online]. Available: https://sensorex.com/blog/2016/05/09/ph-sensor-calibration/

[81] S. Amemiya, P. Bühlmann, and K. Odashima, "A generalized model

for apparently "non-nernstian" equilibrium responses of ionophore-based ion-selective electrodes. 1. independent complexation of the ionophore with primary and secondary ions," *Analytical Chemistry*, vol. 75, no. 14, pp. 3329–3339, 2003, pMID: 14570181. [Online]. Available: https://doi.org/10.1021/ac026471g

[82] M. B. Rooney, D. C. Coomber, and A. M. Bond, "Achievement of Near-Reversible Behavior for the [Fe(CN) ₆] ^{3-/4-} Redox Couple Using Cyclic Voltammetry at Glassy Carbon, Gold, and Platinum Macrodisk Electrodes in the Absence of Added Supporting Electrolyte," *Analytical Chemistry*, vol. 72, no. 15, pp. 3486–3491, 2000. [Online]. Available: http://pubs.acs.org/doi/abs/10.1021/ac991464m

[83] G. Keeley and M. Lyons, "The effects of thin layer diffusion at glassy carbon electrodes modified with porous films of single-walled carbon nanotubes," *International Journal of Electrochemical Science*, vol. 4, no. 6, pp. 794–809, 2009, cited By 87. [Online]. Available: https://www.scopus.com/inward/record.uri?eid=2-s2.0-70149123454&partnerID=40&md5=84e7721665815ca0b27f3d1d91dcffbe

[84] F. Van Rossem, T. Kamperman, J. G. Bomer, A. Van Den Berg, S. Le Gac, and M. Boiani, "Novel approach to sense oxygen in solution using short measurement times," *Proceedings of IEEE Sensors*, 2012.

[85] R. M. Tiggelaar, J. W. Berenschot, J. H. De Boer, R. G. Sanders, J. G. Gardeniers, R. E. Oosterbroek, A. Van Den Berg, and M. C. Elwenspoek, "Fabrication and characterization of high-temperature microreactors with thin film heater and sensor patterns in silicon nitride tubes," *Lab on a Chip*, vol. 5, no. 3, pp. 326–336, 2005.